

1 Revised Manuscript - January 15th, 2017

2 Changes are highlighted in yellow.

3

4 **Summertime observations of elevated levels of ultrafine**
5 **particles in the high Arctic marine boundary layer**

6 **Julia Burkart¹, Megan D. Willis¹, Heiko Bozem², Jennie L. Thomas³, Kathy Law³,**
7 **Peter Hoor², Amir A. Aliabadi⁴, Franziska Köllner⁵, Johannes Schneider⁵, Andreas**
8 **Herber⁶, Jonathan P. D. Abbatt¹, W. Richard Leitch⁷.**

9 [1] {Department of Chemistry, University of Toronto, Toronto, Canada}

10 [2] {Institute of Atmospheric Physics, Johannes Gutenberg-University, Mainz, Germany}

11 [3] {LATMOS/IPSL, UPMC Univ. Paris 06 Sorbonne Universités, UVSQ, CNRS, Paris,
12 France}

13 [4] {Environmental Engineering Program, University of Guelph, Guelph, Canada}

14 [5] {Particle Chemistry Department, Max Planck Institute for Chemistry, Mainz, Germany}

15 [6] {Alfred Wegener Institute, Helmholtz Center for Polar and Marine Research, Bremerhaven,
16 Germany}

17 [7] {Environment and Climate Change Canada, Toronto, Ontario, Canada}

18

19 Correspondence to: J. Burkart (jburkart@chem.utoronto.ca)

20

21 **Abstract**

22 **Motivated by increasing levels of open ocean in the Arctic summer and the lack of prior**
23 **altitude-resolved studies, extensive aerosol measurements were made during 11 flights of the**
24 **NETCARE July 2014 airborne campaign from Resolute Bay, Nunavut. Flights included vertical**
25 **profiles (60 to 3000 m above ground level) over open ocean, fast ice, and boundary layer clouds**
26 **and fogs. A general conclusion, from observations of particle numbers between 5 and 20 nm in**

27 diameter (N_{5-20}), is that ultrafine particle formation occurs readily in the Canadian high Arctic
28 marine boundary layer, especially just above ocean and clouds, reaching values of a few
29 thousand particles/cm³. By contrast ultrafine particle concentrations are very much lower in the
30 free troposphere. Elevated levels of larger particles (for example, from 20 to 40 nm in size, N_{20-}
31 $_{40}$) are sometimes associated with high N_{5-20} , especially over low clouds, suggestive of aerosol
32 growth. The number densities of particles greater than 40 nm in diameter ($N_{>40}$) are relatively
33 depleted at the lowest altitudes, indicative of depositional processes that will lower the
34 condensation sink and promote new particle formation. The number of cloud condensation nuclei
35 (CCN, measured at 0.6% supersaturation) are positively correlated with the numbers of small
36 particles (down to roughly 30 nm), indicating that some fraction of these newly formed particles
37 are capable of being involved in cloud activation. Given that the summertime marine Arctic is a
38 biologically active region, it is important to better establish the links between emissions from the
39 ocean and the formation and growth of ultrafine particles within this rapidly changing
40 environment.

41

42 **1 Introduction**

43 Surface temperatures within the Arctic are rising almost twice as fast as in any other region of
44 the world. As a manifestation of this rapid change the summer sea ice extent has been retreating
45 dramatically over the past decades with the possibility that the Arctic might be ice free by the
46 end of this century (Boé et al., 2009) or even earlier (Wang and Overland, 2012). Arctic aerosol
47 is well known to show a distinct seasonal variation with maximum mass concentrations and a
48 strong long-range anthropogenic influence in winter and early spring. The phenomenon, known
49 as Arctic Haze, was identified many years ago (e.g. Barrie, 1986; Heintzenberg, 1980; Rahn et
50 al., 1977; Shaw, 1995), and has commanded renewed attention in recent years (e.g. Law et al.,
51 2014; Quinn et al., 2007). During summer the Arctic is more isolated from remote anthropogenic
52 sources and represents a comparatively pristine environment. The reason is that the Arctic front
53 (e.g. Barrie, 1986), which provides a meteorological barrier for lower-level air mass exchange,
54 moves north of many source regions during the summer months. Anthropogenic and biomass
55 burning aerosols are transported to the Arctic during the summer, but increased aerosol
56 scavenging helps maintain the pristine conditions near the surface (e.g. Browse et al., 2012; Croft
57 et al., 2016a; Garrett et al., 2011).

58 Zhang et al. (2010) discuss the impacts of declining sea ice on the marine planktonic ecosystem,
59 which includes increasing emissions of dimethyl sulfide (DMS) that may contribute to particle
60 formation in the atmosphere (e.g. Charlson et al., 1987; Pirjola et al., 2000). Enhanced secondary
61 organic aerosol from emissions of biogenic volatile organic compounds is also a possibility (Fu
62 et al., 2009). Primary emissions of aerosol particles from the ocean, such as sea salt and marine
63 primary organic aerosol, may also increase (Browse et al., 2014). Open water tends to increase

64 cloudiness, which means that aerosol influences on clouds are likely to be more important. Over
65 the Arctic the effects of aerosols on clouds are especially uncertain. Models have predicted that
66 increasing numbers of particles may lead to overall warming (Garrett, 2004) when the
67 atmosphere exists in a particularly low particle number state now referred to being "CCN
68 limited" (Mauritsen et al., 2011), to an overall cooling effect when increasing numbers of
69 particles are added to an atmosphere with more particles already present (Lohmann and Feichter,
70 2005; Twomey, 1974). It is important to characterize particle size distributions in this pristine
71 environment to provide a baseline against which future measurements can be compared in a
72 warming world. Indeed, Carslaw et al. (2013) highlight the need to understand pre-industrial-like
73 environments with only natural aerosols in order to reduce the uncertainty in estimations of the
74 anthropogenic aerosol radiative forcing.

75 Primary sources, gas-to-particle formation processes, cloud processing, atmospheric aging,
76 mixing and deposition are all reflected in the size distribution. Therefore, measurements of
77 aerosol size distributions are important for understanding the processes particles undergo in
78 addition to their potential effects on clouds. The presence of ultrafine particles indicates recent
79 production as their lifetime is on the order of hours. We focus this paper on ultrafine particles as
80 these are an indication for in-situ aerosol production processes in the Arctic. We also consider
81 the growth of newly formed particles, as that determines how important they are for climate.

82 Aerosol size distributions including ultrafine particles ($dp < 20$ nm) have been measured before
83 at different locations throughout the Arctic. Long term studies at ground stations such as Alert,
84 Nunavut (Leaith et al., 2013), Ny Alesund and Zeppelin (Engvall et al., 2007; Ström et al.,
85 2003, 2009; Tunved et al., 2013), both on Svalbard and very recently in Tiksi, Russia (Asmi et
86 al., 2016) and Station Nord, Greenland (Nguyen et al., 2016) indicate a strong seasonal
87 dependence of the size distribution with the accumulation mode aerosol dominating during the
88 winter months and a shift to smaller particles during the summer months. New particle formation
89 events are frequently observed from June to August. Ström et al. (2003) show that the size
90 distribution undergoes a rapid change from an accumulation mode dominated distribution during
91 the winter months to an Aitken mode dominated distribution at the beginning of summer. Total
92 number concentrations increase at the beginning of summer and roughly follow the incoming
93 solar radiation on a seasonal scale suggesting that photochemistry is an important factor for new
94 particle formation in the Arctic. At Ny Alesund maximum number concentrations occur in late
95 summer and are explained by the Siberian tundra being a potential source of aerosol precursor
96 gases (Ström et al., 2003) and **marine biogenic sulphur (Heintzenberg and Leck, 1994)**. Analysis
97 of air mass patterns for this region show that the shift in the size distributions is also
98 accompanied by a change of source areas, with a dominance of Eurasian source areas in winter
99 and North Atlantic air during summer (Tunved et al., 2013).

100 Particle measurements including aerosol size distributions were also conducted from ice breaker
101 cruises such as from the Swedish ice breaker Oden (Bigg and Leck, 2001; Covert et al., 1996;

102 Heintzenberg and Leck, 2012; Leck and Bigg, 2005; Tjernström et al., 2014) and the Canadian
103 Coast Guard Ship ice breaker Amundsen (e.g. Chang et al., 2011). Chang et al. (2011) used
104 model calculations to show that the appearance of ultrafine particles can be explained by
105 nucleation and growth attributed to the presence of high atmospheric and oceanic DMS
106 concentrations measured at the same time. The Oden expeditions focus on the pack-ice-covered
107 high Arctic, mainly north of 80N and also confirm the frequent presence of an UFP mode (e.g.
108 Covert et al., 1996). The observations from the Oden cruises offer evidence that UFP in the inner
109 Arctic might originate from primary sources (e.g. Heintzenberg et al., 2015; Karl et al., 2013).
110 This is motivated by three main observations. First, a lack of sulfuric acid components in
111 collected 15-50 nm particles (Leck and Bigg, 1999). Second, Leck and Bigg (2010) highlight
112 that nucleation events in the high Arctic do not follow the classical banana shaped growth curve
113 (Kulmala et al., 2001) but enhanced levels of ultrafine particles rather appear simultaneously in
114 distinct size ranges (Karl et al., 2012). Third, such events could not be modelled with the selected
115 empirical nucleation mechanism for the extremely low DMS concentrations in this region (Karl
116 et al., 2013). As a primary source marine microgels are suggested that might become airborne via
117 the evaporation of fog and cloud droplets (Heintzenberg et al., 2006; Karl et al., 2013).

118 So far most studies that include size distribution measurements in the summertime Arctic were
119 conducted from ground stations or ship cruises. To date there are only two studies that assess the
120 altitude dependence of the size distribution:, i.e. one in the area of Svalbard (Engvall et al., 2008)
121 and one from the Oden performing vertical profiles with a helicopter (Kupiszewski et al., 2013).
122 Although no size distribution measurements were performed, Heintzenberg et al. (1991)
123 measured vertical profiles of the total particle number concentration greater than 10 nm during
124 June and July, 1984 over the Fram Strait-Spitsbergen area, and found a “rather uniform
125 distribution” with altitude. Their measurements, however, were confined to 500 m-MSL and
126 above.

127 In this study we present data from aerosol size distribution measurements taken from an aircraft
128 during a three week period in July 2014 in the high Arctic area of Resolute Bay, Nunavut,
129 Canada. The flights focused on vertical profiles from as low as 60 m above the ground up to
130 3km, as well as on low-level flights above different terrain such as fast ice, open ocean, polynyas
131 and clouds. We focus especially on UFP (5-20 nm in diameter) and address the following
132 questions: What are the concentrations of UFPs in the Arctic summertime, and what is their
133 vertical distribution? What are the environmental conditions that favour occurrence of UFPs?
134 And, is there evidence for growth of UFP to CCN sizes? Aside from the studies conducted near
135 Svalbard, we believe this is the first aircraft study in the high Arctic to systematically address
136 these specific questions. This work provides a comprehensive picture of UFPs observed during
137 the campaign whereas a prior publication from Willis et al., (2016) detailed one UFP formation
138 and growth event observed over Lancaster Sound.

139

140 2 Experimental

141 2.1 Sampling Platform Polar 6

142 The research aircraft Polar 6 owned by the Alfred Wegener Institute, Helmholtz Center for Polar
143 and Marine Research, Bremerhaven, Germany served as the sampling platform. The Polar 6 is a
144 converted DC-3 airplane (Basler BT-67) modified to work under extreme cold weather
145 conditions. An advantage of the plane is that flights at very relatively low speeds and altitudes
146 (< 60 m a.g.l.) are possible. The cabin of the aircraft is non-pressurized. We maintained a
147 constant survey speed of approximately 120 knots (222 km h^{-1}) for measurement flights at
148 constant altitude, and ascent and descent rates of 150 m min^{-1} for vertical profiles. Instruments
149 and measurements specific to this paper are described below.

150 2.1.1 Inlets

151 Aerosol was sampled through a stainless steel inlet mounted to the top of the plane and ahead of
152 the engines to exclude contamination. The tip of the inlet consisted of a shrouded diffuser that
153 provided nearly isokinetic flow. Inside the cabin the intake tubing was connected to a stainless
154 steel tube (outer diameter of 2.5 cm, inner diameter of 2.3 cm) that carried the aerosol to the back
155 of the aircraft where it was allowed to freely exhaust into the cabin so that the system was not
156 over-pressured. The stainless steel tube functioned as a manifold, off which angled inserts were
157 used to connect sample lines to the various instruments described below. In-flight air was pushed
158 through the line with a flow rate of approximately 55 L min^{-1} determined by the sum of the flows
159 drawn by the instruments (35 L min^{-1}), plus the flow measured at the exhaust of the sampling
160 manifold (20 L min^{-1}). A flow of 55 L min^{-1} was estimated to meet nearly isokinetic sampling
161 criteria at survey speed and the transmission of particles through the main inlet was
162 approximately unity for diameters between 20 nm to $1 \mu\text{m}$ (Leaitch et al., 2016). Although the
163 transfer of the aerosol from outside to the instruments is relatively fast (5 seconds or less),
164 volatilization of some components of the particles may have occurred. However, the growth of
165 newly formed particles by organic condensation occurs primarily by low volatility organic
166 components (e.g. Pierce et al., 2012). Thus, the integrity of the smaller particles is likely to have
167 been maintained. We do expect increasing line losses of particles with sizes decreasing from 10
168 nm. Therefore our observations will underestimate N_{5-20} .

169 Trace gases (CO and H_2O) were sampled through a separate inlet made of a 0.4 cm (outer
170 diameter) Teflon tube entering the aircraft at the main inlet and exiting through a rear-facing 0.95
171 cm exhaust line that provided a lower line pressure. The sample flow of approximately 12 L min^{-1}
172 was continuously monitored.

173 2.2 Instrumentation

174 2.2.1 Meteorological parameters and state parameters

175 Aircraft state parameters and meteorological measurements were performed with an AIMMS-20
176 manufactured by Aventech Research Inc. at a very high sampling frequency ($>40\text{Hz}$). The
177 AIMMS-20 consists of three modules: (1) The Air Data Probe that measures the three-
178 dimensional aircraft-relative flow vector (true air speed, angle-of-attack, and sideslip), and
179 turbulence with a three-dimensional accelerometer. As well, temperature and humidity sensors
180 are contained within this unit and provide an accuracy and resolution of 0.30 and 0.01 C for
181 temperature and 2.0 and 0.1% for relative humidity measurements. (2) An Inertial Measurement
182 Unit that consists of three gyros and three accelerometers providing the aircraft angular rate and
183 acceleration; (4) A Global Positioning System for aircraft 3D position and inertial velocity.
184 Horizontal and vertical wind speeds were measured with accuracies of 0.50 and 0.75 m s^{-1} ,
185 respectively. The high frequency raw data were processed to 1Hz resolution. Further details of
186 the AIMMS including data processing can be found in (Aliabadi et al., 2016a).

187 2.2.2 Aerosol physical and chemical properties

188 Particle number concentrations and particle size distributions were measured with a TSI 3787
189 water-based ultrafine Condensation Particle Counter (UCPC), a Droplet Measurement
190 Technology (DMT) Ultra High Sensitivity Aerosol Spectrometer (UHSAS) and a Brechtel
191 Manufacturing Incorporated (BMI) Scanning Mobility System (SMS) coupled with a TSI 3010
192 Condensation Particle Counter (CPC). The UCPC detected particle concentrations of particles
193 larger than 5nm in diameter with a time resolution of 1 Hz. The flow rate was set to 0.6 L min^{-1} .
194 The particle concentrations measured by the UCPC are referred to as N_{tot} hereafter, noting as
195 above that diffusional losses of particles smaller than 10 nm make the N_{tot} observations lower
196 limits.

197 The BMI SMS was set to measure particle size distributions from 20nm to 100nm with a sample
198 flow of 1 L min^{-1} and a sheath flow of 6 L min^{-1} . The duration of one scan was 40 s with a 20 s
199 delay time before each scan resulting in a time resolution of 1min. The UHSAS performed size
200 distribution measurements from 70 nm – 1 μm at a time resolution of 1 Hz with a sample flow
201 rate of 55 $\text{cm}^3 \text{min}^{-1}$. Details of the calibrations and instrument inter-comparisons performed
202 prior and during the campaign are described in detail in Leitch et al. (2016).

203 Cloud condensation nuclei (CCN) were measured with a DMT CCN Counter (CCNC). The
204 CCNC was operated behind a constant pressure inlet that was set to 650 hPa. The nominal
205 supersaturation was held constant at 1%. Calibrations prior and during the campaign (for details
206 see Leitch et al. 2016) showed that a nominal supersaturation of 1% at the reduced pressure
207 translated into 0.6% effective supersaturation.

208 Cloud droplet sizes from 2-45 μm were measured using a wing mounted Particle Measuring
209 System (PMS) FSSP 100. In this study these data are only used to identify periods when the
210 aircraft was flying in cloud. To avoid possible artefacts produced from shattering of cloud
211 droplets at the aerosol inlet, data from in-cloud times are discarded for the purposes of this study.

212 A DMT Single Particle Soot Photometer (SP2) was deployed to measure refractory black carbon
213 (rBC) number and mass concentrations. We refer to rBC mass concentrations as an indication of
214 pollution influence. Calibrations with Aquadag soot were performed prior to and during the
215 campaign. The lower size limit of detection of rBC particles by the SP2 was approximately
216 80nm.

217 Sub-micron aerosol composition was measured with an Aerodyne high-resolution time-of-flight
218 aerosol mass spectrometer (HR-ToF-AMS; e.g. DeCarlo et al., 2006). A detailed description of
219 the instrument is found in Willis et al. 2016. The main purpose of the instrument was to measure
220 non-refractory particulate matter such as sulfate, nitrate, ammonium, methane sulfonic acid
221 (MSA) and the sum of organics. Detection limits were 0.009, 0.008, 0.004, 0.005 and 0.08 $\mu\text{g m}^{-3}$,
222 respectively, for a 30 second averaging time.

223

224 2.2.3 Trace gases

225 Carbon monoxide (CO) was measured with an Aerolaser ultra-fast carbon monoxide monitor
226 model AL 5002 based on VUV fluorimetry, employing the excitation of CO at 150 nm. In-situ
227 calibrations were performed during flight at regular intervals (15 – 30 min) using a NIST
228 traceable CO standard with zero water vapor concentration. CO mixing ratios were used as a
229 relative indicator of aerosol influenced by pollution sources.

230 Water vapour (H_2O) measurements were based on infrared absorption using a LI-7200 enclosed
231 $\text{CO}_2/\text{H}_2\text{O}$ Analyzer from LI-COR Biosciences GmbH. The measurement uncertainty is ± 15
232 ppm_v . H_2O mixing ratios were used to calculate relative humidity with pressure and temperature
233 measured by the AIMMS-20.

234 2.3 Data analysis and nomenclature of particle size data

235 All particle data were averaged to 1 min intervals to match the time resolution of the BMI SMS.
236 Particle concentrations within different size intervals were calculated. The notation N_{a-b} is used;
237 “a” gives the lower limit and “b” the upper limit of the calculated size interval. The BMI SMS
238 was used to determine concentrations of particles from 20-90 nm diameter, and concentrations of
239 particles larger than 90 nm diameter were determined by the UHSAS. If the size interval is
240 expressed as $N_{>a}$ the upper limit is given by the detection limit of the UHSAS (1 μm).
241 Additionally, particle concentrations from 5-20 nm (short: N_{5-20}) were obtained by subtracting

242 particle concentrations measured by the BMI SMS and by the UHSAS from the N_{tot} as
243 determined by the CPC. The N_{5-20} are also referred to as ultrafine particles (UFP) in this study.

244 In order to obtain vertical profiles the data were averaged within altitude intervals. An average
245 profile for a single flight was obtained by binning all data from the respective flight into altitude
246 intervals of 100m starting at the lowest flight altitude. In addition to data obtained during vertical
247 profile flights, data acquired while flying at a constant level were also included. Average profiles
248 containing data from more than one flight were calculated by averaging the respective single
249 flight profiles.

250 Average size distributions were obtained by simply averaging each bin for the desired time and
251 altitude range. The size distributions measured by the BMI SMS were used for particle sizes
252 from 20-90 nm, and the distributions at larger sizes are taken from the UHSAS. All particle
253 concentrations are expressed for ambient pressure conditions, i.e. they have not been adjusted to
254 standard temperature and pressure conditions. The N_{5-20} referred to as UFP are added to the size
255 distributions as additional bin assuming a bin width of 15 nm (from 5-20 nm) with the mid
256 diameter of 12nm.

257

258 **2.4 FLEXPART-WRF Simulations**

259 We used FLEXPART-WRF (Brioude et al., 2013, website: flexpart.eu/wiki/FpLimitedareaWrf)
260 simulations run backwards in time to analyse the origins of air masses sampled along the flight
261 tracks. FLEXPART-WRF is a Lagrangian particle dispersion model based on FLEXPART (Stohl
262 et al., 2005). Meteorological information is obtained from the Weather Research and Forecasting
263 (WRF) Model (Skamarock et al., 2005). FLEXPART-WRF outputs retroplume information such
264 as the residence time of air (over a unit area) prior to sampling. Residence times were integrated
265 over the entire atmospheric column and 7 days backward in time. FLEXPART-WRF was run in
266 two ways. First, one FLEXPART-WRF was completed for each flight using particle releases
267 every 2 minutes along the flight track (100 m x 100 m x 100 m centered on the aircraft location)
268 to produce potential emissions sensitivities (PES) that represent the average air mass origin for
269 each flight. Second, separate runs were completed for points (every 10 minutes) along the flight
270 track (100 m x 100 m x 100 m, 60 second release duration) in order to study different air masses
271 measured during the same flight. A more detailed description of the model as used for
272 NETCARE 2014 is provided by Wentworth et al. (2015).

273

274 **2.5 Study area and flight tracks**

275 From July 4th to July 21st, 2014 eleven flights were conducted out of Resolute Bay (74.7 N, 95.0
276 W). In Figure 1 a compilation of all flight tracks on a satellite image is shown. The satellite
277 picture was taken on July 4th, 2014 and reflects the situation of the region during period I (July 4
278 to July 12). Resolute Bay proved to be an ideal location for this study as we had access to both
279 open ocean and ice covered regions. Additionally two polynyas were located north of Resolute
280 Bay within the reach of our aircraft. Flights ranged between 4-6 hours. The flights covered two
281 main areas: Lancaster Sound east of Resolute Bay and the area north of Resolute Bay where two
282 polynyas were located. The flights south of Resolute Bay in Lancaster Sound concentrated
283 around the ice edge.

284 The ice/water coverage visible on the satellite picture is representative for the area during the
285 first period. As can be seen, the ice edge was situated about 150 km east of Resolute Bay. It is
286 clearly visible in the satellite image as a sharp line. The transition from a completely ice covered
287 region to open ocean was very abrupt during the first period. Only after a period of bad weather
288 with high winds did the ice edge become less clear, and the region starting about 80 km east of
289 Resolute Bay to about 200 km east was covered by fractured ice.

290 Roughly 50% of the flight time was within the inversion layer, and 50% was in the free
291 troposphere conducting altitude profile flights. A considerable amount of time was spent at 2800
292 m as this was the preferred altitude when travelling to a certain area. When clouds were present,
293 the aircraft sampled them by slant profiling through the cloud in the case clouds were above the
294 boundary layer, or, in the case clouds were within 200 m of the surface, by descending into the
295 cloud as low as possible. Aerosol observations while inside cloud are excluded from the analysis
296 here due to potential artifacts from droplets shattering on the outside inlet.

297

298 **3 Meteorological and atmospheric conditions**

299 Meteorological conditions changed over the course of the campaign. Similar conditions were
300 encountered during the first part of the campaign (July 4th – July 12th, 6 flights), referred to as the
301 “Arctic air mass period” because air masses from within the Arctic dominated and the
302 atmosphere showed structures typical for the Arctic such as a low boundary layer height with
303 thermally stable conditions, indicated by a near surface temperature inversion, and frequent
304 formation of low level clouds. At this time Resolute Bay was under the influence of high
305 pressure systems. Clear sky with few or scattered clouds and low wind speeds dominated.
306 Conditions changed starting from July 13th when the region was influenced by troughs of a low
307 pressure system located to the west above Beaufort Sea, which eventually passed through
308 Resolute Bay on July 15th bringing along humidity, precipitation and fog. Intense fog and low
309 visibility impeded flying from July 13th to July 16th. A short good weather window in which the
310 fog dissipated permitted flying again on July 17th (referred to as “transition day”; one flight) just

311 before Resolute Bay came under influence of a pronounced low pressure system located to the
312 south with its center around King William Island (69.0 N, 97.6 W). The last campaign days
313 (referred to as “southern air mass period”, three flights) were characterised by the influence of
314 this pronounced low pressure system bringing air masses from the south and providing higher
315 wind speeds, an overcast sky and occasional precipitation.

316
317 Vertical profiles of median temperature, relative humidity (RH), wind speed, CO and N_{tot} (Figure
318 2) illustrate median atmospheric conditions during the measurement flights. Prominent features
319 representing the trend of each period and reflecting the general meteorological situation will be
320 described here, with details discussed in the respective sections. The Arctic air mass period was
321 characterized by frequent thermally stable conditions within the near surface layer, representing
322 typical conditions during the Arctic summertime (Aliabadi et al., 2016a; Tjernström et al., 2012).
323 The median temperature profiles show that on average the boundary layer reached up to ~300 m
324 with a temperature increase of about 5 C. In this paper we will refer to this part of the
325 atmosphere as the boundary layer (BL) and to the air masses above as the free troposphere (FT).
326 A BL height of 300m corresponds well to the boundary layer height of 275 +/- 164 m estimated
327 by (Aliabadi et al., 2016a) using the method of bulk Richardson number (Aliabadi et al., 2016b)
328 and a critical bulk Richardson number of 0.5, using data from radiosondes launched at Resolute
329 Bay and the Amundsen icebreaker, which also performed research operations in Lancaster sound
330 during the campaign period.

331 Within the BL particle concentrations spanned over a wide range of concentrations (max N_{tot} :
332 ~10000; median values: ~150 to ~1700 cm^{-3}). Highest N_{tot} occurred during the Arctic air mass
333 period, while N_{tot} was constantly low within the lower atmosphere on the transition day. Median
334 temperatures near the surface ranged from -1 C to 5 C during the Arctic air mass period, largely
335 depending on the terrain below (e.g. ice or open water) and were clearly higher during when the
336 southern air masses arrived (e.g. at the “surface”: 4 C and 7 C, respectively) and, if present, the
337 BL was less pronounced. The higher temperatures coincide with the influence of low pressure
338 systems bringing warmer air masses from the west and south and additional higher wind speeds
339 providing a better mixing of the atmospheric layers (5.6 ms^{-1} vs 12 m^{-1} near the surface). CO
340 mixing ratios were extremely low during the Arctic air mass period (median: 78.3 ppb_v) and on
341 the transition day (median: 83.4 ppb_v) indicating pristine air masses that had not recently been
342 affected by pollution or biomass burning sources. During the southern air mass influence CO
343 mixing ratios clearly increased (median: 95.0 ppb_v) confirming a change in air mass and
344 suggesting possible influences by pollution sources and wild fires in the North West Territories
345 (Supplementary Figure 2). Relative humidity profiles show that the near surface layer of the
346 atmosphere was very moist with $\text{RH} > 80 \%$ during all periods.

347

348 4 Results and Discussion

349 4.1 Ultrafine particle events

350 4.1.1 Frequency of ultrafine particle events

351 Throughout the campaign we observed large variability in particle concentrations (Figure 3). We
352 observed not only very clean air masses with N_{tot} of a few tens cm^{-3} (with the lowest 1-second
353 value of 1 cm^{-3}), but also concentrations as high as a few thousands per cm^{-3} (with the highest
354 value of 10000 cm^{-3}). The highest and lowest concentrations were measured within the BL
355 (Figure 3b). Above the BL (Figure 3b) particle concentrations were relatively constant where
356 60% of the time concentrations were between $200 - 300 \text{ cm}^{-3}$ (for a discussion of the average size
357 distribution see sections 4.1.2 - 4.1.4). Especially during the Arctic air mass period (Figure 2) the
358 atmosphere was characterized by a strong contrast between the BL and the FT.

359 UFP were very frequently present within the BL in high concentrations (Figure 3c). Here we
360 refer to "bursts" of particles as a sudden and relatively large increase in N_{5-20} : concentrations
361 suddenly rising from tens cm^{-3} to several hundreds and thousands cm^{-3} . This may reflect
362 inhomogeneities in the NPF process or reflect the aircraft flying in and out of areas of high UFP
363 concentrations. Bursts of $N_{5-20} > 2000/\text{cm}^3$ were observed over polynyas, consistent with
364 previous observations (Leitch et al., 1984; 1994), in Lancaster Sound and south of Resolute
365 Bay. The N_{5-20} was higher than 200 cm^{-3} during 65% of the time. Indeed, high N_{tot} was mainly
366 driven by UFP (as can be seen by comparison of black dots indicating high N_{tot} in Figure 3c and
367 high UFP in Figure 3d). Whenever N_{tot} is greater than 2000 cm^{-3} , UFP was larger than 1000 cm^{-3} .
368 This is also illustrated by the ratio of $\text{UFP}/N_{\text{tot}}$ (Figure 3e). A ratio of zero means that no UFP
369 were present, while a ratio of one means that only UFP were present. Within the boundary layer
370 32% of the time the size distribution was dominated by UFP (ratio > 0.5).

371 The frequent presence of UFP agrees well with other studies made during the Arctic summertime
372 at several locations, such as at the ground stations in Ny Alesund and Zeppelin (Ström et al.,
373 2009; Tunved et al., 2013), at Alert (Leitch et al., 2013), and from ship-based observations
374 (Chang et al., 2011; Covert et al., 1996; Heintzenberg et al., 2006). However, such a frequent
375 presence of an UFP mode (65% of the time $> 200 \text{ cm}^{-3}$) in the BL is unique to this study.
376 Possible reasons for the higher occurrence of UFP might be the combination of the proximity of
377 open ocean (providing a source of UFP or precursor gases), favourable meteorological
378 conditions (sunny weather, inversion layer with cloud formation) and very clean air masses with
379 low condensation sinks. Also, since observations of UFP were one focus of this study, the
380 fractional occurrence of the UFP mode may be biased slightly high due to longer sampling times
381 associated with UFP occurrence. Calm weather conditions may have been another factor. The
382 highest concentrations of UFP were measured at lower wind speeds ($< 5 \text{ m s}^{-1}$; Supplementary
383 Figure 1), while lower UFP concentrations (1000 cm^{-3}) were found at higher wind speeds

384 ($>12\text{ms}^{-1}$) suggesting a dilution effect of the wind. Such a dilution effect implies proximity to the
385 source.

386 In the following sections, the vertical distribution of UFP and the size distributions are discussed
387 in relation to meteorological conditions during the three distinct periods that characterized this
388 campaign.

389

390 4.1.2 Arctic air mass period: July 4th to July 12th

391 During this first period the study area was under the influence of a high pressure system. As
392 illustrated by FLEXPART-WRF results (Figure 4a and 4b), air masses were either coming from
393 the North extending to the east in the Arctic Ocean or from the East passing over the open ocean
394 in Lancaster Sound and Baffin Bay. Both examples indicate that air masses resided within the
395 Arctic region at least 5 days prior to sampling. This is true for all flights during this period. The
396 very low CO mixing ratios (78 ppb_v, see Figure 2) and average BC mass concentrations of 3 ng
397 m⁻³ (not shown) confirm that air masses were very clean and without recent influence from
398 pollution sources. As discussed in section 3, temperature profiles indicate thermally stable
399 conditions in the lowest layers with near-surface temperature inversions. During almost all
400 vertical profiles we observed temperature inversions of about 4-6 C near the surface. Such an
401 atmospheric structure i.e. a shallow boundary layer is typical for the Arctic summertime (e.g.
402 Aliabadi et al., 2016a; Tjernström et al., 2012).

403 The Arctic air mass period was characterized by a very sharp contrast between the BL and the
404 FT in terms of particle number concentrations and sizes (Figure 5). The BL was characterized by
405 a prominent layer of UFP from the surface to about 300 m with the highest concentrations closest
406 to the surface (Figure 5a). The height of the UFP layer coincides with the average height of the
407 temperature inversion for this period (see temperature profile Figure 2) and indicates that air
408 masses were stably layered limiting exchange with the FT. This is supported by the observed
409 lower turbulent mixing (i.e. turbulent kinetic energy) from boundary layer to the free troposphere
410 during the campaign (Aliabadi et al., 2016a).

411 During this period we measured the highest concentrations of UFPs with the one minute average
412 up to 5300 cm⁻³. On a typical flight several bursts (see Section 4.1.1) of high UFP concentrations
413 were encountered in the BL. Particle bursts lasted from a few seconds to several minutes,
414 corresponding to a spatial extent of several hundreds of meters to dozens of kilometers. The large
415 spatial variability is also illustrated by the frequency distribution of UFP in the BL shown in
416 Figure 5c: 40% of the time concentrations of UFP were larger than 200 cm⁻³, 11% of the time
417 larger than 1000 cm⁻³ and 3% of the time even larger than 2000 cm⁻³. Particle concentrations in
418 the FT are relatively uniform, and concentrations of UFP were less than 50 cm⁻³ up to 1200m and
419 $\sim 10\text{ cm}^{-3}$ above.

420 The average N_{20-40} is similar to the UFP, showing a maximum in its concentration at the same
421 altitude. The concentrations of larger particles ($N_{>40}$, $N_{>80}$, $N_{>150}$) are much lower in the clean BL
422 (surface areas of $\sim 5\mu\text{m}^2 \text{m}^{-3}$ and lower). However, the $N_{>40}$ and $N_{>80}$ increase from the lowest
423 altitude to the next averaged altitude, consistent with the increase in the UFP and N_{20-40} . These
424 results suggest that some of the UFP experienced growth to sizes of 20-80 nm within a few
425 hours, as demonstrated by Willis et al. (2016). Within the FT particle concentrations were
426 surprisingly uniform and concentrations of UFP were less than 50 cm^{-3} up to 1200m and $\sim 10 \text{ cm}^{-3}$
427 above.

428 In Figure 5b, the median size distribution shows that increases in UPF in the BL were frequent.
429 The average size distribution shows that at times higher concentrations of particles extended up
430 to about 80 nm, consistent with the suggestion above that some UFP particles experienced
431 growth to larger sizes. A relevant case will be discussed in Section 4.3. Occasionally a mode of
432 particles larger than 400 nm was present in the BL over open water (see Section 4.2), which was
433 likely the product of primary oceanic emissions.

434

435 4.1.3 Transition day on July 17th

436 July 17th marks the transition from dominance by Arctic air masses to a more distant influence
437 from southern air masses. The transition day consists of only one flight in the area of Lancaster
438 Sound, during which low concentrations of particles larger than 20 nm were observed below 600
439 m: e.g. $N_{>40}$ ranged from 60 cm^{-3} to 100 cm^{-3} ; see Figure 6. The deeper layer of lower
440 concentrations may have been a result of cloud processing and scavenging. During the days
441 before flying was impossible because of intense fog and cloud at Resolute Bay. A different
442 transport regime may also have contributed to this situation. On this day the low pressure system
443 situated to the west was bringing air masses from the west along the Canadian and Alaskan
444 coastline (Figure 4c). The temperature profile shows an inversion between 650-1000m possibly
445 indicating a change in air mass. CO mixing ratios (83ppb_v) and BC mass concentrations ($3\text{ng}/\text{cm}^{-3}$)
446 were also quite low indicating mostly Arctic background conditions.

447 On this day, occasional bursts of UFP up to $1400\text{-}1900 \text{ cm}^{-3}$ were observed within the boundary
448 layer (Figure 6b). UFP of 200 cm^{-3} or more were observed about 20% of the time (Figure 6c),
449 and the average concentration was 240 cm^{-3} at the lowest level of the profile (Fig. 6a).
450 Concentrations of larger particles ($N_{>40}$, $N_{>80}$, $N_{>150}$) increased sharply at about 700m coinciding
451 with the temperature inversion. The very low concentrations of larger particles ($N_{>150}$: $<10 \text{ cm}^{-3}$)
452 below the temperature inversion are very similar to the conditions encountered within the BL
453 during the previous period. As above, the differences in the transition day below 700 m may
454 have been due to a combination of fog/cloud scavenging and a change of air mass. Median and
455 average size distributions indicate a minimum at around 65nm that might be the result of cloud

456 processing (Hoppel et al., 1994), consistent with the Arctic observations of (Heintzenberg et al.,
457 2006) and the activation diameters observed during this study (Leaitch et al., 2016).

458 4.1.4 Southern air mass period: July 19th – July 21st

459 During this period the region was under the influence of a low pressure system centered south of
460 Resolute Bay. FLEXPART-WRF air mass trajectories (Figures 4d and 4e) indicate a prevalence
461 of air masses from the south potentially affected by wild fires (see Supplementary Figure 2). At
462 the beginning of this period on July 19th (Figure 4d), air mass trajectories suggest the strongest
463 influence from the south while towards the end of the period on July 21st (Figure 4e),
464 FLEXPART-WRF indicates that southern air masses mixed with air masses coming off
465 Greenland. Near surface temperatures were higher than during the previous periods (Figure 2)
466 and temperature inversions were less pronounced (2-4 C) and not observed at all locations
467 suggesting a less stable lower atmosphere. On July 19th we encountered the highest wind speeds
468 in the BL (16 m/s within the near surface layer and 20 m/s slightly above). Also RH was
469 relatively high near the surface (91%) and did not drop below 80% throughout the vertical
470 atmosphere. CO mixing ratios were higher than during the prior periods suggesting that the air
471 was at times influenced by pollution or biomass burning.

472 UFP were observed less frequently than during the Arctic air mass period and in lower
473 concentrations (Figure 7). Bursts of UFP above 1000 cm⁻³ occurred only at three locations, all
474 during the flight on July 21st. Average UFP concentrations were only approximately 190 cm⁻³.
475 UFP concentrations of 200 cm⁻³ or higher were detected 31% of the time below 300m (Figure
476 7c).

477 The southern air mass period clearly shows different aerosol characteristics within the near
478 surface layer than compared to the Arctic air mass period and the transition day. Average
479 concentrations of particles larger than 40 nm were highest within the boundary layer and
480 decreased with altitude (Figure 7a). This is in sharp contrast to the cleaner boundary layers
481 observed before. Whereas concentrations of particles larger 40nm were ~100 cm⁻³ and lower
482 during both prior periods, they were as high as 300 cm⁻³ for this period. Even large accumulation
483 mode particles (N_{>150}) averaged ~50 cm⁻³ (compared to 10 cm⁻³ for both previous periods). Also,
484 both the median and average size distributions show a pronounced mode of particles larger than
485 500 nm within the BL (Figure 7b). Primary emissions from the sea spray promoted by the higher
486 surface wind speeds (see Figure 2) are likely a factor contributing to the larger particles.

487 During the southern air mass period, three important factors had changed compared to both prior
488 periods. (1) Air mass back trajectories had clearly shifted to the south and potentially transported
489 emissions from wild fires located in the Northwest Territories (Supplementary Figure 2) into the
490 region, which might mix into the boundary layer. (2) The Amundsen ice breaker was present in
491 Lancaster Sound and acted as a local pollution source. (3) Wind speeds were higher and the
492 ocean was visibly turbulent with breaking waves that might enhance primary oceanic aerosol

493 emissions. The increased condensation sinks from these potential sources in combination with
494 other factors (e.g. reduced sun light) and relatively low residence times of air masses within the
495 boundary layer (compared to the Arctic air mass period) may explain the relatively low and
496 infrequent concentrations of UFPs.

497 Within the FT the size distributions shows a bimodal character with a minima at 60-80 nm,
498 which may indicate the air masses experienced cloud processing. This is likely, given the
499 presence of the low pressure system bringing moister and warmer air masses. The bimodal size
500 distribution is different from the average size distribution during the Arctic air mass period when
501 drier air masses from within the Arctic dominated.

502 **4.2 UFP occurrence above ice versus water**

503 We investigated the potential influence of different underlying water surfaces on the occurrence
504 of UFP by examining in detail the time periods when we were flying at altitudes at or below 500
505 m during the Arctic air mass period. We distinguish between three water surfaces: ice covered
506 areas (including ice edge and ice covered with melt ponds), open ocean (including polynyas),
507 and low-level clouds (including both cloud above water and cloud above ice). Here we point out
508 that the case “cloud” does not include in-cloud flight times but only flight periods when above
509 cloud top without actually entering the cloud (confirmed by a zero signal in a liquid cloud probe
510 (FSSP100)). An altitude of 500 m was chosen to include time periods when we were flying
511 above low-level clouds and to capture mostly flights within the boundary layer where a local
512 influence of the terrain below was likely. During the Arctic air mass period, there was a clear
513 separation between ice and open water over Lancaster Sound with east of the ice edge
514 completely ice free, while west of the ice edge the ocean was seamlessly covered by fast ice (see
515 satellite picture in Figure 1).

516 Each average profile above the different water surface exhibits unique features (Figure 8). Above
517 ice the highest concentrations of UFP (average: 400 cm^{-3}) were found nearer the surface (70 m)
518 and the N_{tot} are slightly higher (580). In the BL over open water, the N_{tot} and UFP number
519 concentrations are 900 cm^{-3} and 560 cm^{-3} , respectively, and in the air just above cloud, the
520 average N_{tot} and UFP number concentrations are 2000 cm^{-3} and 1040 cm^{-3} , respectively. In the
521 open water and cloud cases, the highest concentrations of ultrafines are at the point of
522 measurement closest to the water surface. In the cloud case and open water case, the N_{20-40}
523 particles show an increase at the same time as the N_{tot} and UFP suggesting that the UFP form and
524 grow to larger sizes. This is not observed in the over-ice case, which suggests that some of the
525 new particles could have formed elsewhere (e.g. over open water) and been transported over the
526 ice, or that the growth rates over ice are slow. In all three cases, the largest particles show
527 relatively smaller abundances at the lowest altitudes samples. An increased abundance of UFP at
528 lower surface areas supports the hypothesis that UFP form via nucleation of precursor gases.

529 4.3 Case study: July 8

530 The flight on July 8 provides a case study illustrating that the occurrence of UFP is confined to
531 the BL suggesting a surface source of UFP and that the appearance of UFP is promoted by cloud.
532 We consider the altitude dependence of the UFP within the BL in relation to air mass history and
533 cloud.

534 On this flight we first flew out into Lancaster Sound west of Resolute Bay, turned around and
535 descended into the BL above the ice. Here, we focus on the time period from 15:50 UTC
536 (descent into the BL) to 17:20 UTC where we travelled from west to east and remained within
537 the BL but stayed out of cloud as shown in Figure 9; see also Supplementary Figure 2. The later
538 part of the flight focused on in-situ cloud properties and is discussed elsewhere (Leitch et al.,
539 2016). The weather was sunny with low level clouds starting around 150 km over ice and west of
540 the ice edge in Lancaster Sound. The clouds had formed over the water and were blown over the
541 ice where they were dissipating (Leitch et al., 2016). In the entire area the atmosphere was
542 characterized by a surface temperature inversion extending vertically up to about 300 m with ~1
543 C near the surface and ~5 C at 300 m and was accompanied by decreasing relative humidity
544 (Figure 9f). Local low-level winds were predominantly from the south to east and wind speeds
545 were below 5 ms⁻¹.

546 UFP were present throughout the BL with the highest concentrations at the lowest altitudes and
547 decreasing concentrations towards the top of the BL (Figure 9b). In contrast, larger particles (e.g.
548 N_{>40}) exhibit the opposite pattern, with lower concentrations at lower altitudes and higher
549 concentrations at higher altitudes. Six locations from west to east (points A-F in Figure 9a) are
550 used to illustrate the changing aerosol characteristics. Location A is situated well above the BL
551 and at this point no UFP were present (detailed size distributions are shown in Supplementary
552 Figure 4). At location B, the point at which we first entered the BL, an UFP mode (~370 cm⁻³)
553 was present at 60m, while UFP concentrations were lower at slightly higher altitudes (~80 cm⁻³
554 at 230 m) such as location C. At the lower altitudes the UFP concentrations gradually increased
555 as we approached the ice edge. The most striking observation is the steep increase in particle
556 concentrations at about 60 km west of the ice edge (location D) where UFP increased to above
557 4000 cm⁻³ at 150 m or just above cloud top. At the same time N₂₀₋₄₀ concentrations showed a
558 similar increase. The increased UFP concentrations were vertically limited to near cloud top and
559 decreased rapidly with increasing altitude. The same pattern is also observed for temperature,
560 H₂O and CO₂ (Figure 9g) suggesting the existence of a distinct air mass at the surface that gets
561 diluted into the air mass above. Further east the flight was restricted to a slightly higher altitude
562 above cloud top. At point F, where we were close to the BL top, no peaks in particle
563 concentrations were observed. At point E, just before the ice edge, between the top of cloud and
564 the top of the BL, UFP concentrations reached about 3400 cm⁻³.

565 Air mass histories at these locations determined from FLEXPART-WRF (Figure 10) indicate the
566 following:

567 (1) To the west of Resolute Bay (point B) Lancaster Sound air masses had been mixed with air
568 masses from the North. This is also confirmed by the local wind directions indicating winds
569 coming from the Northwest sector (Figure 10a), and it is consistent with the associated change in
570 cloud. (2) Near the top of the BL, air masses had descended recently (< 3 h) into the BL (Figure
571 10c point C and point F). (3) In contrast, deeper within the BL at points B and D air masses had
572 descended into the BL earlier (~ 20 h) before arriving at the point of observation. In the case of
573 point D, where we observed the largest mode of UFP extending above 40nm, air masses had
574 been travelling from the east exclusively over the open waters in Lancaster Sound during the last
575 day before arriving at the point of observation.

576 Aerosol composition shows a clear difference between the aerosol in the FT and the BL. The
577 aerosol sulphate rapidly decreases as we enter the BL around 16:00, while aerosol organic **mass**
578 **concentrations** show an initial relative increase followed by an absolute increase towards the east
579 (Figure 9c). Within the BL aerosol organics and sulphate mass loadings show a pattern similar to
580 $N_{>40}$ and $N_{>80}$. Both decrease each time we descended deeper into the BL. However, at the same
581 time the organics-to-sulphate ratio indicates that the relative contribution of organics to aerosol
582 mass increases at lower altitudes and especially above cloud (Figure 9e). Well within the
583 inversion layer and in the vicinity of cloud top the aerosol was dominated by organics. At the
584 same time also ratio of MSA to sulphate was higher (Figure 9e), suggesting a marine biogenic
585 influence of the aerosol sulphur. The marine biogenic influence at the lower altitudes agrees well
586 with the FLEXPART-WRF simulations showing that air masses at this altitude had spent almost
587 an entire day exposed to the open waters in Lancaster Sound. Consistent with the higher organic
588 content measured with the AMS, the single particle aerosol mass spectrometer ALABAMA
589 (Brands et al., 2011; Willis et al., 2016) detected a higher fraction of trimethylamine (TMA)-
590 containing particles for particles larger than 150 nm in diameter (F. Köllner, personal
591 communication, July 2016). Gaseous TMA emissions from marine biogenic origin (Ge et al.,
592 2011; Gibb et al., 1999) may have additionally favored the subsequent growth of the freshly
593 nucleated particles by condensation. Another possibility may be uptake of TMA in the cloud
594 phase (Rehbein et al., 2011) if the particles have grown to sufficiently large sizes to be activated
595 as CCN. Interestingly, compared to other days these TMA-containing particles are smaller and to
596 a lesser degree internally mixed with potassium and levoglucosan which supports the hypothesis
597 of ultrafine particles originating from nucleation in a biogenic marine environment and
598 subsequent growth.

599 To explain these observations, we hypothesize that the smaller particle mode is formed by
600 nucleation and growth occurring within the BL and especially in cloud vicinity. UFP
601 concentrations near cloud top have been reported before (e.g. Radke and Hobbs 1991,
602 Wiedensohler et al. 1997, Clarke et al., 1999; Garrett et al., 2002; Hegg et al., 1990; Mauldin et

603 al., 1997) and it is suggested that nucleation in near cloud regions is favoured by the low surface
604 areas, possibly due to cloud scavenged aerosol, moist air and a high actinic flux. Indeed, near
605 cloud top where we observed an increase of UFP extending up to almost 50 nm the conditions
606 for nucleation and growth are ideal. We speculate that the availability of precursor gases is
607 provided by the long residence time (~20h) of the air masses over open water (Figure 10, point
608 D). **In other words, precipitating clouds scavenge aerosol particles, reducing the surface area for
609 condensation, but some fraction of nucleation precursor gases with lower Henry's Law constants
610 can pass through (e.g. SO₂) leaving the potential for H₂SO₄ in the higher OH in the cloud
611 outflow (a discussion of the processes can be found in Seinfeld and Pandis, 1998).** The very high
612 organic loadings and MSA to sulphate ratio likely indicate that the formation and growth of these
613 particles is driven by a combination of DMS and organic precursors (volatile organic
614 compounds) that are emitted by the open ocean in Lancaster Sound (e.g. Chang et al., 2011;
615 Sjostedt et al., 2012; Mungall et al., 2016).

616 The event at point E occurs where the aircraft was between cloud top and the top of the BL,
617 where no increases in UFP were observed before or after. It may be that the aircraft descended
618 slightly but sufficiently into the cloud-influenced area, which looks to be 25-40 m above cloud
619 top (Figure 9g), but also at that point we were in vicinity of Prince Leopold Island which is a bird
620 sanctuary and many bird colonies nest at the 260m high cliff. FLEXPART-WRF and the in-situ
621 wind measurement show that air masses to a large extent were directly coming off the island
622 (Figure 10, point E) suggesting a connection between the appearance of UFP and possible
623 emissions from the fauna of the island. The increase of particle phase ammonium (Figure 9d) at
624 the same time supports this connection and nucleation of particles from biogenic precursors
625 emitted by bird colonies are documented (Weber et al., 1998; Wentworth et al., 2016, Croft et al.
626 2016b).

627 Alternatively, it should be considered that evaporating fog and cloud droplets may also act as a
628 primary source of UFP (e.g. Heintzenberg et al., 2006; Karl et al., 2013; Leck and Bigg, 1999).
629 Karl et al., (2013) suggested a combined pathway that involves the emission of UFP by fog and
630 cloud droplets, together with secondary processes enabling growth of these particles. For our
631 observations we have no reason to assume that nucleation does not occur since conditions are
632 ideal but we cannot rule out that nanoparticles are emitted by the possibly evaporating cloud
633 droplets onto which gases then condense.

634 In conclusion the aerosol mass within the near surface layer is dominated by organics relative to
635 sulphate, while at just slightly higher altitude sulphate is clearly increased and increases further
636 above the inversion layer. A high organic content coincides with increases in UFP particles,
637 especially at times when also growth into the size range up to 50nm is indicated. Similarly the
638 MSA-to-sulphate ratio shows a peak at the lowest altitudes with maximum values in the vicinity
639 of clouds that coincide with a long residence time (~20h) of the air masses within the BL and
640 above open water. The data thereby suggest a marine biogenic influence of the aerosol within the

641 lower layers of the atmosphere. We note that similarly high levels of aerosol organics and MSA
642 were observed during the flight on July 12 associated with a NPF event and growth but in cloud-
643 free conditions Willis et al. (2016).

644 **4.4 CCN activity**

645 CCN concentrations were measured at a supersaturation of 0.6%. The vertical profiles of CCN
646 concentrations (Figure 11a) show patterns similar to those of larger particles. In the very clean
647 boundary layer of the Arctic air mass period and the transition day CCN concentrations are
648 equally low ($\sim 70 \text{ cm}^{-3}$ and $\sim 50 \text{ cm}^{-3}$, respectively). In contrast, southern air mass period average
649 BL CCN concentrations are amongst the highest observed during this campaign ($>300 \text{ cm}^{-3}$).
650 Within the free troposphere CCN concentrations are surprisingly constant during the Arctic air
651 mass period ($120 \pm 27 \text{ cm}^{-3}$) and more variable on the transition day ($92 \pm 46 \text{ cm}^{-3}$) and the
652 southern air mass period ($103 \pm 67 \text{ cm}^{-3}$). The constant CCN concentrations during the Arctic air
653 mass period correspond to the very uniform atmosphere dominated by aged aerosols we
654 observed during this period and to the more layered atmosphere influenced by southern air
655 masses possibly contaminated by biomass burning plumes during the later period. Correlations
656 with $N_{>80}$ (Figure 11b) confirm that larger particles are a good approximation for these CCN
657 concentrations. On average CCN concentrations agree to within $\pm 20 \%$ of $N_{>80}$. However, it
658 should be noted that slight differences between the 3 periods are indicated in the correlation
659 curves: during the Arctic air mass period the average activation diameters are smaller than 80
660 nm, and during the southern air mass period they are larger than 80 nm. Assuming uniform
661 chemical composition throughout the particle size range, an activation diameter of 80 nm at 0.6%
662 supersaturation indicates an aerosol much less hygroscopic than, for example, ammonium
663 sulphate; pure ammonium sulphate particles would activate at 40 nm at 0.6% supersaturation. For
664 the one specific event during which growth occurred (Willis et al., 2016), it was demonstrated
665 that high CCN concentrations coincide with elevated organic mass loading. The reduced
666 hygroscopicity of organic material relative to soluble inorganic salts (Petters and Kreidenweis,
667 2007) can explain the larger effective activation diameter.

668 A central question is whether and to what degree the CCN are influenced by the UFP. Two
669 factors help with addressing this question: 1) particles as small as 20 nm and in general much
670 smaller than the average 80 nm size associated with the CCN at 0.6% will nucleate cloud
671 droplets in the clean environment of the summer Arctic (Leaith et al., 2016); 2) there is
672 evidence here that increases in particles larger than 20 nm are associated with increases in the
673 UFP, particularly for UFP influenced by cloud (e.g. Figure 8). Figure 12 shows regressions of
674 CCN with UFP, $N_{>20}$, $N_{>30}$, $N_{>40}$ and $N_{>50}$. The high variability in the UFP and the time needed
675 for a UFP particle to grow to an average size of 80 nm under these low precursor levels does not
676 permit a direct connection of the CCN and UFP, but in all other cases, the main clusters of the
677 regressions show quite similar and strong connections with the CCN measurements.

678 Associations of the UFP with the $N_{>20}$ in the BL mean that some of these UFP are able to
679 contribute to cloud-nucleating particles.

680

681 **5 Discussion and Conclusions**

682 This study presents airborne observations of ultrafine particles (UFP) during the Arctic
683 summertime. Eleven flights were conducted in July 2014 in the area of Resolute Bay situated in
684 the Canadian Archipelago. The location allowed access to open water, ice-covered regions and
685 low clouds. Flights focused around the ice edge in Lancaster Sound including open waters to the
686 east, the ice-covered region to the west, and polynas north of Resolute Bay. UFP were observed
687 within all regions and above all terrains with the highest concentrations encountered in the
688 boundary layer immediately above cloud and open water. It is shown that UFP occur most
689 frequently (>65 % of the time) and with the highest concentrations (up to 5300 cm^{-3}) during an
690 Arctic air mass period when the air is very clean and the boundary layer is thermally stable.

691 The frequent presence of UFP in the boundary layer over open water and low cloud and the
692 enhanced number concentrations at the lowest altitudes sampled indicate a surface source, such
693 as the ocean, for the UFP gaseous precursors. This is especially true during the Arctic air mass
694 period when the sampling region was pristine and not influenced by pollution. FLEXPART-
695 WRF simulations indicate that air masses had resided within the Arctic region at least 5-7 days
696 prior to sampling. During this time UFP were restricted to the boundary layer and no UFP events
697 were observed aloft, thereby excluding that these UFP form in the free troposphere and subside
698 into the near surface layer e.g. (Clarke et al., 1998; Quinn and Bates, 2011). At the same time we
699 observed an extremely clean boundary layer (surface area of $N_{>40} \sim 5 \mu\text{m}^2\text{m}^{-3}$). Low surface areas
700 increase the probability of particle formation via nucleation by reducing the surfaces for
701 precursor gases to condense on.

702 Chlorophyll-a concentrations (Supplementary Figure 5) indicate a relatively high level of
703 biological activity of the ocean (such as phytoplankton blooms known to produce DMS)
704 throughout Lancaster Sound, to the east in Baffin Bay and in the open waters of the polynyas
705 during the time period of the study. Indeed, measurements in Lancaster Sound performed from
706 the Amundsen ice breaker just a few days after the aircraft campaign show that gas-phase DMS
707 mixing ratios were high in the Lancaster Sound region (Mungall et al., 2016), up to 1155 ppt_v.
708 DMS was also measured from the Polar 6 aircraft with an offline technique. Maximum mixing
709 ratios of 110 ppt_v were detected in the surface layer (R. Ghahremaninezhad; personal
710 communication), again confirming a marine influence in the boundary layer. The measured DMS
711 concentrations are above the nucleation threshold obtained by modelling performed in the study
712 of Chang et al. (2011) who concluded that DMS mixing ratios of $\geq 100\text{ppt}_v$ are sufficient to
713 account for the formation of hundreds of UFP when background particle concentrations are low.

714 Relating observations of UFP to the surface below during the Arctic air mass period revealed
715 that the highest UFP concentrations occurred above low-level cloud and open water with
716 averages of 1040 cm^{-3} and 560 cm^{-3} , respectively. Above low-level cloud N_{20-40} showed
717 increased concentrations. This simultaneous increase in concentrations suggests that UFP grow
718 into the 40 nm size range, where they can nucleate cloud droplets.

719 Overall, the summertime Arctic is an active region in terms of new particle formation,
720 occasionally accompanied by growth. The value of these altitude profiles across a wide spatial
721 extent, performed for the first time in this campaign, is that they demonstrate that this activity is
722 largely confined to the boundary layer, and that the dominant source of small particles to the
723 boundary layer does not arise by mixing from aloft but most likely from marine sources. For
724 future studies, the relative impact of such natural sources of UFP needs to be evaluated with
725 respect to potential new sources, such as may arise with increasing shipping.

726

727 **Acknowledgements**

728 The authors would like to thank a large number of people for their contributions to this work. We
729 thank Kenn Borek Air, in particular the pilots Kevin Elke and John Bayes and the aircraft
730 engineer Kevin Riehl. We are grateful to John Ford, David Heath and the University of Toronto
731 machine shop for safely mounting our instruments on racks for aircraft deployment. We thank
732 Jim Hodgson and Lake Central Air Services in Muskoka, Jim Watson (Scale Modelbuilders,
733 Inc.), Julia Binder and Martin Gerhmann (Alfred Wegener Institute, Helmholtz Center for Polar
734 Marine Research, AWI), Mike Harwood and Andrew Elford (Environment and Climate Change
735 Canada, ECCC), for their support of the integration of the instrumentation and aircraft. We
736 gratefully acknowledge Carrie Taylor (ECCC), Bob Christensen (U of T), Lukas Kandora,
737 Manuel Sellmann and Jens Herrmann (AWI), Desiree Toom, Sangeeta Sharma, Dan Veber,
738 Andrew Platt, Anne Marie Macdonald, Ralf Staebler and Maurice Watt (ECCC) for their support
739 of the study. We thank the Biogeochemistry department of MPIC for providing the CO
740 instrument and Dieter Scharffe for his support during the preparation phase of the campaign. The
741 authors J.L. Thomas and K.S. Law acknowledge funding support from the European Union
742 under Grant Agreement n_ 5265863 – ACCESS (Arctic Climate Change, Economy and Society)
743 project (2012-2015) and TOTAL SA. Computer simulations were performed on the IPSL
744 mesoscale computer center (Mésocentre IPSL), which includes support for calculations and data
745 storage facilities. We thank the Nunavut Research Institute and the Nunavut Impact Review
746 Board for licensing the study. Logistical support in Resolute Bay was provided by the Polar
747 Continental Shelf Project (PCSP) of Natural Resources Canada under PCSP Field Project
748 #218614, and we are particularly grateful to Tim McCagherty and Jodi MacGregor of the PCSP.
749 Funding for this work was provided by the Natural Sciences and Engineering Research Council
750 of Canada through the NETCARE project of the Climate Change and Atmospheric Research

751 Program, the Alfred Wegener Institute, Helmholtz Center for Polar and Marine Research and
752 Environment and Climate Change Canada.
753

753 **References**

- 754 Aliabadi, A. A., Staebler, R. M., Liu, M. and Herber, A.: Characterization and Parametrization of
755 Reynolds Stress and Turbulent Heat Flux in the Stably-Stratified Lower Arctic Troposphere
756 Using Aircraft Measurements, *Boundary-Layer Meteorol.*, doi:10.1007/s10546-016-0164-7,
757 2016a.
- 758 Aliabadi, A. A., Staebler, R. M., de Grandpré, J., Zadra, A. and Vaillancourt, P. A.: Comparison
759 of Estimated Atmospheric Boundary Layer Mixing Height in the Arctic and Southern Great
760 Plains under Statically Stable Conditions: Experimental and Numerical Aspects, *Atmosphere-*
761 *Ocean*, 54(1), 60–74, doi:10.1080/07055900.2015.1119100, 2016b.
- 762 Asmi, E., Kondratyev, V., Brus, D., Laurila, T., Lihavainen, H., Backman, J., Vakkari, V.,
763 Aurela, M., Hatakka, J., Viisanen, Y., Uttal, T., Ivakhov, V. and Makshtas, A.: Aerosol size
764 distribution seasonal characteristics measured in Tiksi, Russian Arctic, *Atmos. Chem. Phys.*,
765 16(3), 1271–1287, doi:10.5194/acp-16-1271-2016, 2016.
- 766 **Barrie, L. A.: Arctic air pollution: An overview of current knowledge, *Atmos. Environ.*, 20(4),**
767 **643–663, doi:10.1016/0004-6981(86)90180-0, 1986.**
- 768 Bigg, E. K. and Leck, C.: Properties of the aerosol over the central Arctic Ocean, *J. Geophys.*
769 *Res.*, 106(D23), 32101, doi:10.1029/1999JD901136, 2001.
- 770 Boé, J., Hall, A. and Qu, X.: September sea-ice cover in the Arctic Ocean projected to vanish by
771 2100, *Nat. Geosci.*, 2(5), 341–343, doi:10.1038/ngeo467, 2009.
- 772 Brands, M., Kamphus, M., Böttger, T., Schneider, J., Drewnick, F., Roth, a., Curtius, J., Voigt,
773 C., Borbon, a., Beekmann, M., Bourdon, a., Perrin, T. and Borrmann, S.: Characterization of a
774 Newly Developed Aircraft-Based Laser Ablation Aerosol Mass Spectrometer (ALABAMA) and
775 First Field Deployment in Urban Pollution Plumes over Paris During MEGAPOLI 2009, *Aerosol*
776 *Sci. Technol.*, 45(1), 46–64, doi:10.1080/02786826.2010.517813, 2011.
- 777 Brioude, J., Arnold, D., Stohl, A., Cassiani, M., Morton, D., Seibert, P., Angevine, W., Evan, S.,
778 Dingwell, A., Fast, J. D., Easter, R. C., Pisso, I., Burkhardt, J. and Wotawa, G.: The Lagrangian
779 particle dispersion model FLEXPART-WRF version 3.1, *Geosci. Model Dev.*, 6(6), 1889–1904,
780 doi:10.5194/gmd-6-1889-2013, 2013.
- 781 Browse, J., Carslaw, K. S., Arnold, S. R., Pringle, K. and Boucher, O.: The scavenging processes
782 controlling the seasonal cycle in Arctic sulphate and black carbon aerosol, *Atmos. Chem. Phys.*,
783 12(15), 6775–6798, doi:10.5194/acp-12-6775-2012, 2012.
- 784 Browse, J., Carslaw, K. S., Mann, G. W., Birch, C. E., Arnold, S. R. and Leck, C.: The complex
785 response of Arctic aerosol to sea-ice retreat, *Atmos. Chem. Phys.*, 14(14), 7543–7557,
786 doi:10.5194/acp-14-7543-2014, 2014.
- 787 Carslaw, K. S., Lee, L. A., Reddington, C. L., Pringle, K. J., Rap, A., Forster, P. M., Mann, G.
788 W., Spracklen, D. V., Woodhouse, M. T., Regayre, L. A. and Pierce, J. R.: Large contribution of
789 natural aerosols to uncertainty in indirect forcing., *Nature*, 503(7474), 67–71,
790 doi:10.1038/nature12674, 2013.

791 Chang, R. Y. W., Sjostedt, S. J., Pierce, J. R., Papakyriakou, T. N., Scarratt, M. G., Michaud, S.,
792 Levasseur, M., Leaitch, W. R. and Abbatt, J. P. D.: Relating atmospheric and oceanic DMS
793 levels to particle nucleation events in the Canadian Arctic, *J. Geophys. Res. Atmos.*, 116(21), 1–
794 10, doi:10.1029/2011JD015926, 2011.

795 Charlson, R. J., Lovelock, J. E., Andreae, M. O. and Warren, S. G.: Oceanic phytoplankton,
796 atmospheric sulphur, cloud albedo and climate, *Nature*, 326, 655–661, doi:10.1038/326655a0,
797 1987.

798 Clarke, A. D., L, V. J., Eisele, F., Mauldin, R. L., Tanner, D. and M, L.: Particle production in
799 the remote marine atmosphere: Cloud outflow and subsidence during ACE 1, *Earth Sci.*, 103,
800 1998.

801 Clarke, A. D., Kapustin, V. N., Eisele, F. L., Weber, R. J. , and McMurry, P. H.: Particle
802 production near marine clouds: sulfuric acid and predictions from classical binary nucleation,
803 *Geophys. Res. Lett.*, 26, 2425-2428, doi: 10.1029/1999GL900438, 1999.

804 Covert, D. S., Wiedensohler, A., Aalto, P., Heintzenberg, J., McMurry, P. H. and Leck, C.:
805 Aerosol number size distributions from 3 to 500 nm diameter in the arctic marine boundary layer
806 during summer and autumn, *Tellus, Ser. B Chem. Phys. Meteorol.*, 48(2), 197–212, 1996.

807 Croft, B., Martin, R. V., Leaitch, W. R., Tunved, P., Breider, T. J., D’Andrea, S. D. and Pierce, J.
808 R.: Processes controlling the seasonal cycle of Arctic aerosol number and size distributions,
809 *Atmos. Chem. Phys.*, 16, 3665-3682, doi:10.5194/acp-16-3665-2016, 2016a.

810 Croft, B., G.R. Wentworth, R.V. Martin, W.R. Leaitch, J.G. Murphy, B.N. Murphy, J. Kodros,
811 J.P.D. Abbatt and J.R. Pierce. Contribution of Arctic seabird-colony ammonia to atmospheric
812 particles and cloud-albedo radiative effect. *Nat. Commun.* 7, 13444, doi: 10.1038/ncomms13444,
813 2016b.

814 DeCarlo, P. F., Kimmel, J. R., Trimborn, A., Northway, M. J., Jayne, J. T., Aiken, A. C., Gonin,
815 M., Fuhrer, K., Horvath, T., Docherty, K. S., Worsnop, D. R. and Jimenez, J. L.: Field-
816 deployable, high-resolution, time-of-flight aerosol mass spectrometer., *Anal. Chem.*, 78(24),
817 8281–9, doi:10.1021/ac061249n, 2006.

818 Engvall, A.-C., Krejci, R., Ström, J., Minikin, A., Treffeisen, R., Stohl, A. and Herber, A.: In-situ
819 airborne observations of the microphysical properties of the Arctic tropospheric aerosol during
820 late spring and summer, *Tellus B*, 0(0), 080414161623888–???, doi:10.1111/j.1600-
821 0889.2008.00348.x, 2008.

822 Engvall, a.-C., Krejci, R., Ström, J., Treffeisen, R., Scheele, R., Hermansen, O. and Paatero, J.:
823 Changes in aerosol properties during spring-summer period in the Arctic troposphere, *Atmos.*
824 *Chem. Phys.*, 8, 445-462, doi:10.5194/acp-8-445-2008, 2008.

825 Garrett, T. J.: Effects of varying aerosol regimes on low-level Arctic stratus, *Geophys. Res. Lett.*,
826 31(17), L17105, doi:10.1029/2004GL019928, 2004.

827 Garrett, T. J., Hobbs, P. V and Radke, L. F.: High Aitken Nucleus Concentrations above Cloud
828 Tops in the Arctic, *J. Atmos. Sci.*, 59(3), 779–783, doi:10.1175/1520-
829 0469(2001)059<0779:HANCAC>2.0.CO;2, 2002.

830 Garrett, T. J., Brattström, S., Sharma, S., Worthy, D. E. J. and Novelli, P.: The role of
831 scavenging in the seasonal transport of black carbon and sulfate to the Arctic, *Geophys. Res.*
832 *Lett.*, 38(16), 1–6, doi:10.1029/2011GL048221, 2011.

833 Ge, X., Wexler, A. S. and Clegg, S. L.: Atmospheric amines - Part I. A review, *Atmos. Environ.*,
834 45(3), 524–546, doi:10.1016/j.atmosenv.2010.10.012, 2011.

835 Gibb, S. W., Mantoura, R. F. C. and Liss, P. S.: Ocean-atmosphere exchange and atmospheric
836 speciation of ammonia and methylamines in the region of the NW Arabian Sea, *Global*
837 *Biogeochem. Cycles*, 13(1), 161–178, doi:10.1029/98GB00743, 1999.

838 Hegg, D. A., Radke, L. F. and Hobbs, P. V: Particle production associated with marine clouds, *J.*
839 *Geophys. Res. Atmos.*, 95(D9), 13917–13926, 1990.

840 Heintzenberg, B. J.: Particle size distribution and optical properties, *Tellus*, 32, 251–260,
841 10.1111/j.2153-3490.1980.tb00952.x, 1980.

842 Heintzenberg, B., Ström, J., Ogren, J. A., and Fimpel, H.-P.: Vertical profiles of aerosol
843 properties in the summer troposphere of central Europe, scandinavia and the svalbard region,
844 *Atmos. Env.*, 25, 621-627, doi: 10.1016/0960-1686(91)90059-G, 1991.

845 Heintzenberg, B., and Leck, C.: Seasonal variation of the atmospheric aerosol near the top of the
846 marine boundary layer over Spitsbergen related to the Arctic sulphur cycle. *Tellus B*, 46, 52-67,
847 doi: 10.1034/j.1600-0889.1994.00005.x, 1994.

848 Heintzenberg, J., Leck, C., Birmili, W., Wehner, B., Tjernström, M., Wiedensohler, A.,
849 Tjernstrom, M. and Wiedensohler, A.: Aerosol number-size distributions during clear and fog
850 periods in the summer high Arctic: 1991, 1996 and 2001, *Tellus B*, 58(1), 41–50,
851 doi:10.1111/j.1600-0889.2005.00171.x, 2006.

852 Heintzenberg, J. and Leck, C.: The summer aerosol in the central Arctic 1991–2008: did it
853 change or not?, *Atmos. Chem. Phys.*, 12(9), 3969–3983, doi:10.5194/acp-12-3969-2012, 2012.

854 Heintzenberg, J., Leck, C. and Tunved, P.: Potential source regions and processes of aerosol in
855 the summer Arctic, *Atmos. Chem. Phys.*, 15(11), 6487–6502, doi:10.5194/acp-15-6487-2015,
856 2015.

857 Hoppel, W. a., Frick, G. M., Fitzgerald, J. W. and Larson, R. E.: Marine boundary layer
858 measurements of new particle formation and the effects nonprecipitating clouds have on aerosol
859 size distribution, *J. Geophys. Res.*, 99(D7), 14443, doi:10.1029/94JD00797, 1994.

860 Karl, M., Leck, C., Gross, A. and Pirjola, L.: A study of new particle formation in the marine
861 boundary layer over the central Arctic Ocean using a flexible multicomponent aerosol dynamic
862 model, *Tellus B*, 64(0), 1–24, doi:10.3402/tellusb.v64i0.17158, 2012.

863 Karl, M., Leck, C., Coz, E. and Heintzenberg, J.: Marine nanogels as a source of atmospheric
864 nanoparticles in the high Arctic, *Geophys. Res. Lett.*, 40(14), 3738–3743, doi:10.1002/grl.50661,
865 2013.

866 Kulmala, M., Dal Maso, M., Mäkelä, J. M., Pirjola, L., Väkevä, M., Aalto, P., Miikkulainen, P.,
867 Hämeri, K. and O’Dowd, C. D.: On the formation, growth and composition of nucleation mode
868 particles, *Tellus, Ser. B Chem. Phys. Meteorol.*, 53, 479–490, doi:10.1034/j.1600-

869 0889.2001.d01-33.x, 2001.

870 Kupiszewski, P., Leck, C., Tjernström, M., Sjogren, S., Sedlar, J., Graus, M., Müller, M.,
871 Brooks, B., Swietlicki, E., Norris, S. and Hansel, A.: Vertical profiling of aerosol particles and
872 trace gases over the central Arctic Ocean during summer, *Atmos. Chem. Phys.*, 13(24), 12405–
873 12431, doi:10.5194/acp-13-12405-2013, 2013.

874 Law, K. S., Stohl, A., Quinn, P. K., Brock, C. A., Burkhart, J. F., Paris, J. D., Ancellet, G.,
875 Singh, H. B., Roiger, A., Schlager, H., Dibb, J., Jacob, D. J., Arnold, S. R., Pelon, J. and
876 Thomas, J. L.: Arctic air pollution: New insights from POLARCAT-IPY, *Bull. Am. Meteorol.*
877 *Soc.*, 95(12), 1873–1895, doi:10.1175/BAMS-D-13-00017.1, 2014.

878 Leaitch, W.R., Hoff, R.M., Melnichuk, S., and Hogan, W.: Some chemical and physical
879 properties of the Arctic winter aerosol in northeastern Canada. *J. Climate Appl. Meteorol.*, 23,
880 916-928, [http://dx.doi.org/10.1175/1520-0450\(1984\)023<0916:SPACPO>2.0.CO;2](http://dx.doi.org/10.1175/1520-0450(1984)023<0916:SPACPO>2.0.CO;2), 1984.

881 Leaitch, W.R., Barrie, L.A., Bottenheim, J.W., Li, S.-M., Shepson, P. and Yokouchi, Y.:
882 Airborne observations related ozone depletion at polar sunrise. *J. Geophys. Res.*, 99, 25499-
883 25517, 10.1029/94JD02750, 1994.

884 Leaitch, W. R., Sharma, S., Huang, L., Toom-Saunty, D., Chivulescu, A., Macdonald, A. M.,
885 von Salzen, K., Pierce, J. R., Bertram, A. K., Schroder, J. C., Shantz, N. C., Chang, R. Y. W. and
886 Norman, A.-L.: Dimethyl sulfide control of the clean summertime Arctic aerosol and cloud,
887 *Elem. Sci. Anth.*, 1(1), 17, doi:10.12952/journal.elementa.000017, 2013.

888 Leaitch, W. R., Korolev, A., Aliabadi, A. A., Burkart, J., Willis, M., Abbatt, J. P. D., Bozem, H.,
889 Hoor, P., Köllner, F., Schneider, J., Herber, A., Konrad, C. and Brauner, R.: Effects of 20-100
890 nanometre particles on liquid clouds in the clean summertime Arctic, *Atmos. Chem. Phys.*, 16,
891 11107-11124, doi:10.5194/acp-16-11107-2016, 2016.

892 Leck, C. and Bigg, E. K.: Aerosol production over remote marine areas-A new route, *Geophys.*
893 *Res. Lett.*, 26(23), 3577, doi:10.1029/1999GL010807, 1999.

894 Leck, C. and Bigg, E. K.: Source and evolution of the marine aerosol - A new perspective,
895 *Geophys. Res. Lett.*, 32(19), 1–4, doi:10.1029/2005GL023651, 2005.

896 Leck, C. and Bigg, E. K.: New Particle Formation of Marine Biological Origin, *Aerosol Sci.*
897 *Technol.*, 44(7), 570–577, doi:10.1080/02786826.2010.481222, 2010.

898 Lohmann, U. and Feichter, J.: Global indirect aerosol effects: a review, *Atmos. Chem. Phys.*, 5,
899 715–735, doi:10.5194/acp-5-715-2005, 2005.

900 Mauldin, R. L., Madronich, S., Flocke, S. J., Eisele, F. L., Frost, G. J. and Prevot, A. S. H. :
901 New insights on OH: Measurements around and in clouds, *Geophys. Res. Lett.*, 24(No 23),
902 3033-3036, doi:10.1029/97GL02983, 1997.

903 Mauritsen, T., Sedlar, J., Tjernström, M., Leck, C., Martin, M., Shupe, M., Sjogren, S., Sierau,
904 B., Persson, P. O. G., Brooks, I. M. and Swietlicki, E.: An Arctic CCN-limited cloud-aerosol
905 regime, *Atmos. Chem. Phys.*, 11(1), 165–173, doi:10.5194/acp-11-165-2011, 2011.

906 Mungall, E. L., Croft, B., Lizotte, M., Thomas, J. L., Murphy, J. G., Levasseur, M., Martin, R.
907 V., Wentzell, J. J. B., Liggio, J. and Abbatt, J. P. D.: Dimethyl sulfide in the summertime Arctic

908 atmosphere: measurements and source sensitivity simulations, *Atmos. Chem. Phys.*, 16(11),
909 6665–6680, doi:10.5194/acp-16-6665-2016, 2016.

910 Nguyen, Q. T., Glasius, M., Sørensen, L. L., Jensen, B., Skov, H., Birmili, W., Wiedensohler, A.,
911 Kristensson, A., Nøjgaard, J. K. and Massling, A.: Seasonal variation of atmospheric particle
912 number concentrations, new particle formation and atmospheric oxidation capacity at the high
913 Arctic site Villum Research Station, Station Nord, *Atmos. Chem. Phys. Discuss.*, 1–41,
914 doi:10.5194/acp-2016-205, 2016.

915 Petters, M. D. and Kreidenweis, S. M.: A single parameter representation of hygroscopic growth
916 and cloud condensation nucleus activity, *Atmos. Chem. Phys.*, 7, 1961–1971, 2007.

917 Pierce, J. R., Leaitch, W. R., Liggio, J., Westervelt, D. M., Wainwright, C. D., Abbatt, J. P. D.,
918 Ahlm, L., Al-Basheer, W., Cziczo, D. J., Hayden, K. L., Lee, A. K. Y., Li, S.-M., Russell, L. M.,
919 Sjostedt, S. J., Strawbridge, K. B., Travis, M., Vlasenko, A., Wentzell, J. J. B., Wiebe, H. A.,
920 Wong, J. P. S., and Macdonald, A. M.: Nucleation and condensational growth to CCN sizes
921 during a sustained pristine biogenic SOA event in a forested mountain valley, *Atmos. Chem.*
922 *Phys.*, 12, 3147-3163, doi:10.5194/acp-12-3147-2012, 2012.

923 Pirjola, L., O’Dowd, C. D., Brooks, I. M. and Kulmala, M.: Can new particle formation occur in
924 the clean marine boundary layer?, *J. Geophys. Res. Atmos.*, 105(D21), 26531–26546,
925 doi:10.1029/2000JD900310, 2000.

926 Quinn, P. K. and Bates, T. S.: The case against climate regulation via oceanic phytoplankton
927 sulphur emissions, *Nature*, 480(7375), 51–56, doi:10.1038/nature10580, 2011.

928 Quinn, P. K., Shaw, G., Andrews, E., Dutton, E. G., Ruoho-Airola, T. and Gong, S. L.: Arctic
929 haze: Current trends and knowledge gaps, *Tellus, Ser. B Chem. Phys. Meteorol.*, 59(1), 99–114,
930 doi:10.1111/j.1600-0889.2006.00238.x, 2007.

931 Radke, F. L. and Hobbs, P. V.: Humidity and particle fields around some small cumulus clouds,
932 *Journal of atmospheric sciences*, 48(9), 1190-1193, doi: [http://dx.doi.org/10.1175/1520-](http://dx.doi.org/10.1175/1520-0469(1991)048<1190:HAPFAS>2.0.CO;2)
933 [0469\(1991\)048<1190:HAPFAS>2.0.CO;2](http://dx.doi.org/10.1175/1520-0469(1991)048<1190:HAPFAS>2.0.CO;2), 1991.

934 Rahn, K. A., Borys, R. D. and Shaw, G. E.: The Asian source of Arctic haze bands, *Nature*, 268,
935 713-715, doi: 10.1038/268713a0, 1977.

936 Rehbein, P. J. G., Jeong, C. H., McGuire, M. L., Yao, X., Corbin, J. C. and Evans, G. J.: Cloud
937 and fog processing enhanced gas-to-particle partitioning of trimethylamine, *Environ. Sci.*
938 *Technol.*, 45(10), 4346–4352, doi:10.1021/es1042113, 2011.

939 Riipinen, I., Pierce, J. R., Yli-Juuti, T., Nieminen, T., Häkkinen, S., Ehn, M., Junninen, H.,
940 Lehtipalo, K., Petäjä, T., Slowik, J., Chang, R., Shantz, N. C., Abbatt, J., Leaitch, W. R.,
941 Kerminen, V.-M., Worsnop, D. R., Pandis, S. N., Donahue, N. M., and Kulmala, M.: Organic
942 condensation: a vital link connecting aerosol formation to cloud condensation nuclei (CCN)
943 concentrations, *Atmos. Chem. Phys.*, 11, 3865-3878, doi:10.5194/acp-11-3865-2011, 2011.

944 Seinfeld, J.H., and Pandis, S. N.: *Atmospheric Chemistry and Physics: From Air Pollution to*
945 *Climate Change*. 3rd Edition. John Wiley & Sons, Inc., 2016.

946 Shaw, G.E. and Stamnes, K.: Arctic haze: perturbations of the polar radiation budget. *Ann. N. E*

947 Ad. Aci. 338, 533-539, doi: 10.1111/j.1749-6632.1980.tb17145.x 1980.
948

949 Shaw, G. E.: The Arctic Haze Phenomenon, *Bull. Am. Meteorol. Soc.*, 76, 2403–2413,
950 doi:10.1175/1520-0477(1995)076<2403:TAHP>2.0.CO;2, 1995.

951 Skamarock, W. C., Klemp, J. B., Dudhia, J., Gill, D. O., Barker, D. M., Wang, W. and Powers, J.
952 G.: A Description of the Advanced Research WRF Version 2, [online] Available from:
953 <http://oai.dtic.mil/oai/oai?verb=getRecord&metadataPrefix=html&identifier=ADA487419>
954 (Accessed 22 March 2016), 2005.

955 Sjostedt, S. J., Leaitch, W. R., Levasseur, M., Scarratt, M., Michaud, S., Motard-Côté, J.,
956 Burkhardt, J. H., and Abbatt J.: Evidence for the uptake of atmospheric acetone and methanol by
957 the Arctic Ocean during late summer DMS-Emission plumes. *J. Geophys. Res.*, 117, D12303,
958 doi: 10.1029/2011JD017086, 2012.

959 Stohl, a., Forster, C., Frank, A., Seibert, P. and Wotawa, G.: Technical note: The Lagrangian
960 particle dispersion model FLEXPART version 6.2, *Atmos. Chem. Phys. Discuss.*, 5(4), 4739–
961 4799, doi:10.5194/acpd-5-4739-2005, 2005.

962 Ström, J., Umegård, J., Tørseth, K., Tunved, P., Hansson, H. C., Holmén, K., Wismann, V.,
963 Herber, A. and König-Langlo, G.: One year of particle size distribution and aerosol chemical
964 composition measurements at the Zeppelin Station, Svalbard, March 2000-March 2001, *Phys.*
965 *Chem. Earth*, 28(March 2000), 1181–1190, doi:10.1016/j.pce.2003.08.058, 2003.

966 Ström, J., Engvall, A. C., Delbart, F., Krejci, R. and Treffeisen, R.: On small particles in the
967 Arctic summer boundary layer: Observations at two different heights near Ny-Ålesund,
968 Svalbard, *Tellus, Ser. B Chem. Phys. Meteorol.*, 61 B(2), 473–482, doi:10.1111/j.1600-
969 0889.2008.00412.x, 2009.

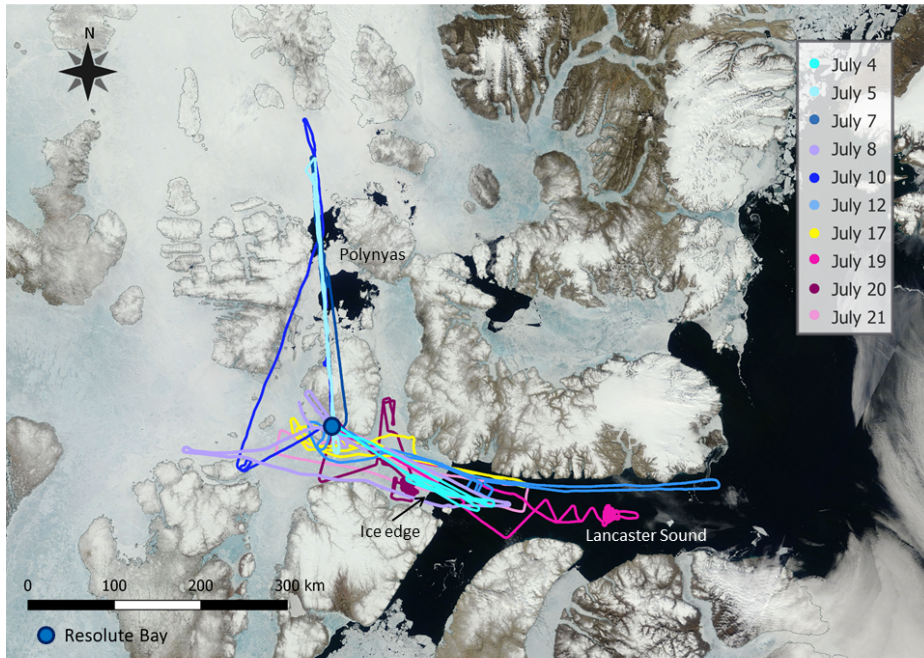
970 Tjernström, M., Birch, C. E., Brooks, I. M., Shupe, M. D., Persson, P. O. G., Sedlar, J.,
971 Mauritsen, T., Leck, C., Paatero, J., Szczodrak, M. and Wheeler, C. R.: Meteorological
972 conditions in the central Arctic summer during the Arctic Summer Cloud Ocean Study
973 (ASCOS), *Atmos. Chem. Phys.*, 12(15), 6863–6889, doi:10.5194/acp-12-6863-2012, 2012.

974 Tjernström, M., Leck, C., Birch, C. E., Bottenheim, J. W., Brooks, B. J., Brooks, I. M., Bäcklin,
975 L., Chang, R. Y. W., De Leeuw, G., Di Liberto, L., De La Rosa, S., Granath, E., Graus, M.,
976 Hansel, a., Heintzenberg, J., Held, a., Hind, a., Johnston, P., Knulst, J., Martin, M., Matrai, P.
977 a., Mauritsen, T., Müller, M., Norris, S. J., Orellana, M. V., Orsini, D. a., Paatero, J., Persson, P.
978 O. G., Gao, Q., Rauschenberg, C., Ristovski, Z., Sedlar, J., Shupe, M. D., Sierau, B., Sirevaag,
979 a., Sjogren, S., Stetzer, O., Swietlicki, E., Szczodrak, M., Vaattovaara, P., Wahlberg, N.,
980 Westberg, M. and Wheeler, C. R.: The Arctic Summer Cloud Ocean Study (ASCOS): Overview
981 and experimental design, *Atmos. Chem. Phys.*, 14(6), 2823–2869, doi:10.5194/acp-14-2823-
982 2014, 2014.

983 Tunved, P., Ström, J. and Krejci, R.: Arctic aerosol life cycle: linking aerosol size distributions
984 observed between 2000 and 2010 with air mass transport and precipitation at Zeppelin station,
985 Ny-Ålesund, Svalbard, *Atmos. Chem. Phys.*, 13(7), 3643–3660, doi:10.5194/acp-13-3643-2013,
986 2013.

- 987 Twomey, S.: Pollution and the Planetary Albedo, *Atmos. Environ.*, 41(Vol. 8), 1251–1256,
988 doi:10.1016/j.atmosenv.2007.10.062, 1974.
- 989 Wang, M. and Overland, J. E.: A sea ice free summer Arctic within 30 years: An update from
990 CMIP5 models, *Geophys. Res. Lett.*, 39(17), 2–6, doi:10.1029/2012GL052868, 2012.
- 991 Weber, R. J., McMurry, P. H., Mauldin, L., Tanner, D. J., Eisele, F. L., Brechtel, F. J.,
992 Kreidenweis, S. M., Kok, G. L., Schillawski, R. D. and Baumgardner, D.: A study of new
993 particle formation and growth involving biogenic and trace gas species measured during ACE 1,
994 *J. Geophys. Res.*, 103(D13), 16385–16396, doi:10.1029/97JD02465, 1998.
- 995 Wentworth, G. R., Murphy, J. G., Croft, B., Martin, R. V., Pierce, J. R., Côté, J.-S., Courchesne,
996 I., Tremblay, J.-É., Gagnon, J., Thomas, J. L., Sharma, S., Toom-Saunty, D., Chivulescu, a.,
997 Levasseur, M. and Abbatt, J. P. D.: Ammonia in the summertime Arctic marine boundary layer:
998 sources, sinks and implications, *Atmos. Chem. Phys.*, 16, 1937-1953, doi:10.5194/acp-16-1937-
999 2016, 2016.
- 1000 Wiedensohler, A., Covert, D. S., Swietlicki, E., Aalto, P., Heintzenberg, J. and Leck, C.:
1001 Occurrence of an ultrafine particle mode less than 20 nm in diameter in the marine boundary
1002 layer during Arctic summer and autumn, *Tellus, Ser. B Chem. Phys. Meteorol.*, 48(2), 213–222,
1003 doi:10.1034/j.1600-0889.1996.t01-1-00006.x, 1996.
- 1004 Wiedensohler, A. H.-C. Hansson, D. Orsini, M. Wendisch, F. Wagner, K.N. Bower, T.W.
1005 Chourolarton, M. Wells, M. Parkin, K. Acker, W. Wiprecht, M.C. Facchini, J.A. Lind, S. Fuzzi,
1006 B.G. Arends, M. Kulmalao: Night-time formation and occurrence of new particles associated
1007 with orographic clouds, *Atmos. Env.*, 31(16), 2445-2559, doi: [http://dx.doi.org/10.1016/S1352-
1008 2310\(96\)00299-3](http://dx.doi.org/10.1016/S1352-2310(96)00299-3), 1997.
- 1009 Willis, M. D., Burkart, J., Thomas, J. L., Köllner, F., Schneider, J., Bozem, H., Hoor, P. M.,
1010 Aliabadi, A. A., Schulz, H., Herber, A. B., Leaitch, W. R. and Abbatt, J. P. D.: Growth of
1011 nucleation mode particles in the summertime Arctic: a case study, *Atmos. Chem. Phys.*, 7663–
1012 7679, doi:10.5194/acp-16-7663-2016, 2016.
- 1013 Zhang, J., Spitz, Y. H., Steele, M., Ashjian, C., Campbell, R., Berline, L. and Matrai, P.:
1014 Modeling the impact of declining sea ice on the Arctic marine planktonic ecosystem, *J. Geophys.*
1015 *Res. Ocean.*, 115(10), 1–24, doi:10.1029/2009JC005387, 2010.
- 1016
- 1017

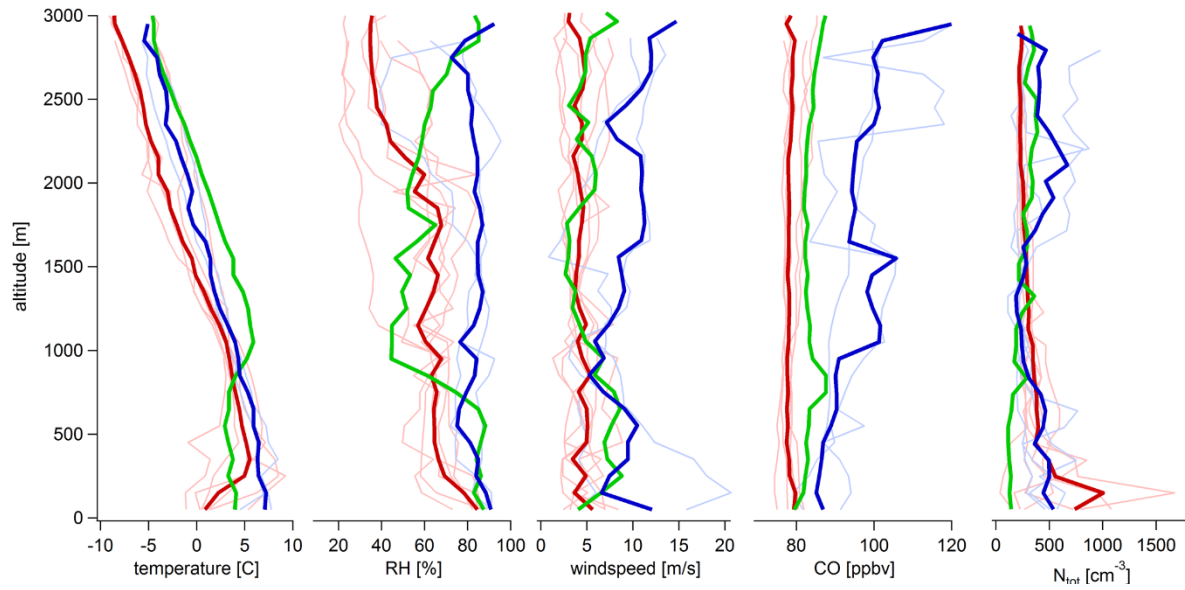
1017
1018



1019
1020
1021
1022

Figure 1. Compilation of all flight tracks plotted on a satellite image from July 4, 2014. The image is taken from: <https://earthdata.nasa.gov/labs/worldview>.

1022



1023

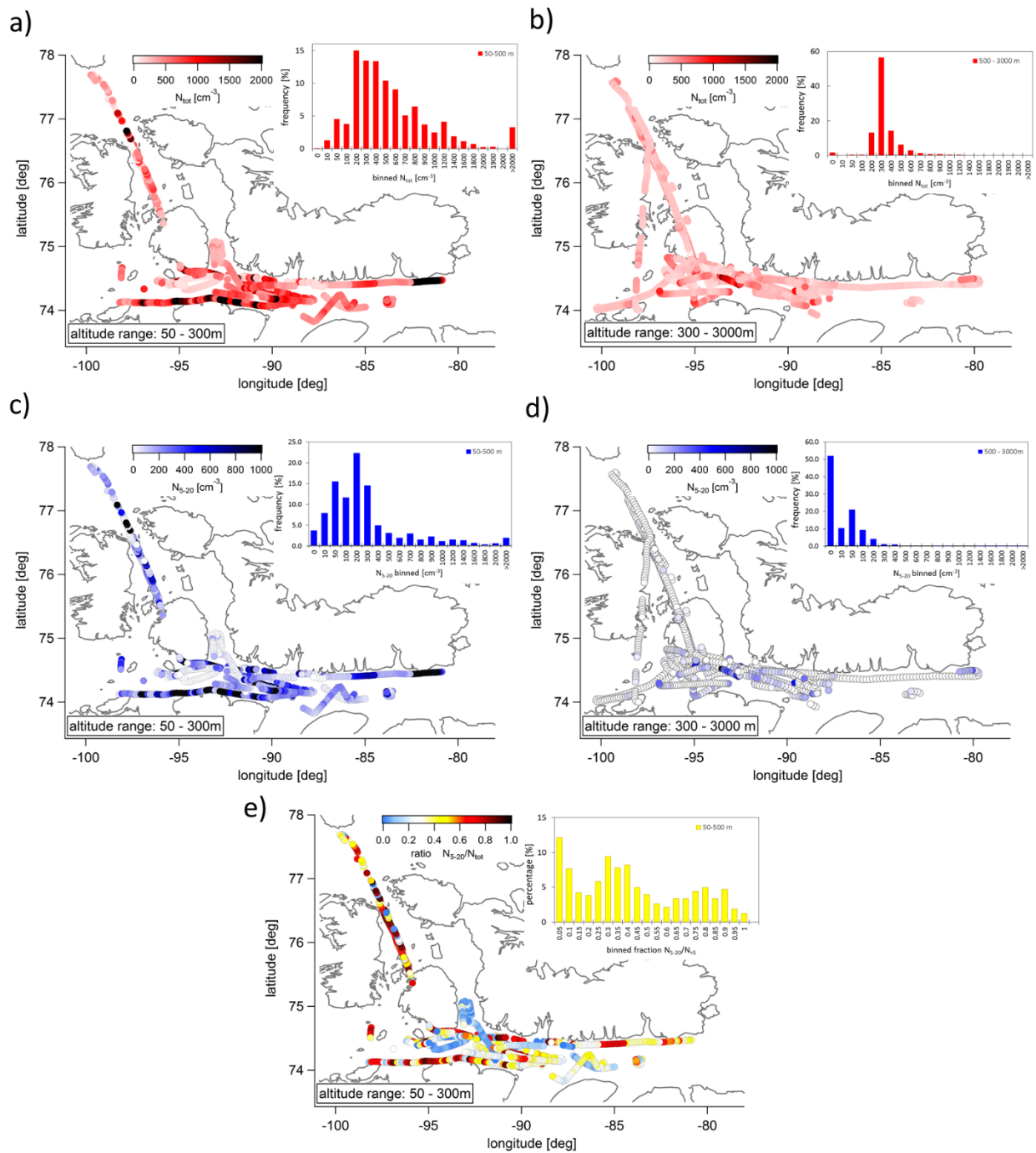
1024 Figure 2. Median temperature, relative humidity (RH), wind speed, CO mixing ratio and N_{tot}
1025 profiles for the Arctic air mass period (dark red), the transition day (dark green), and the southern
1026 air mass period (dark blue). Median profiles for each flight are plotted in the background in the
1027 corresponding light colours.

1028

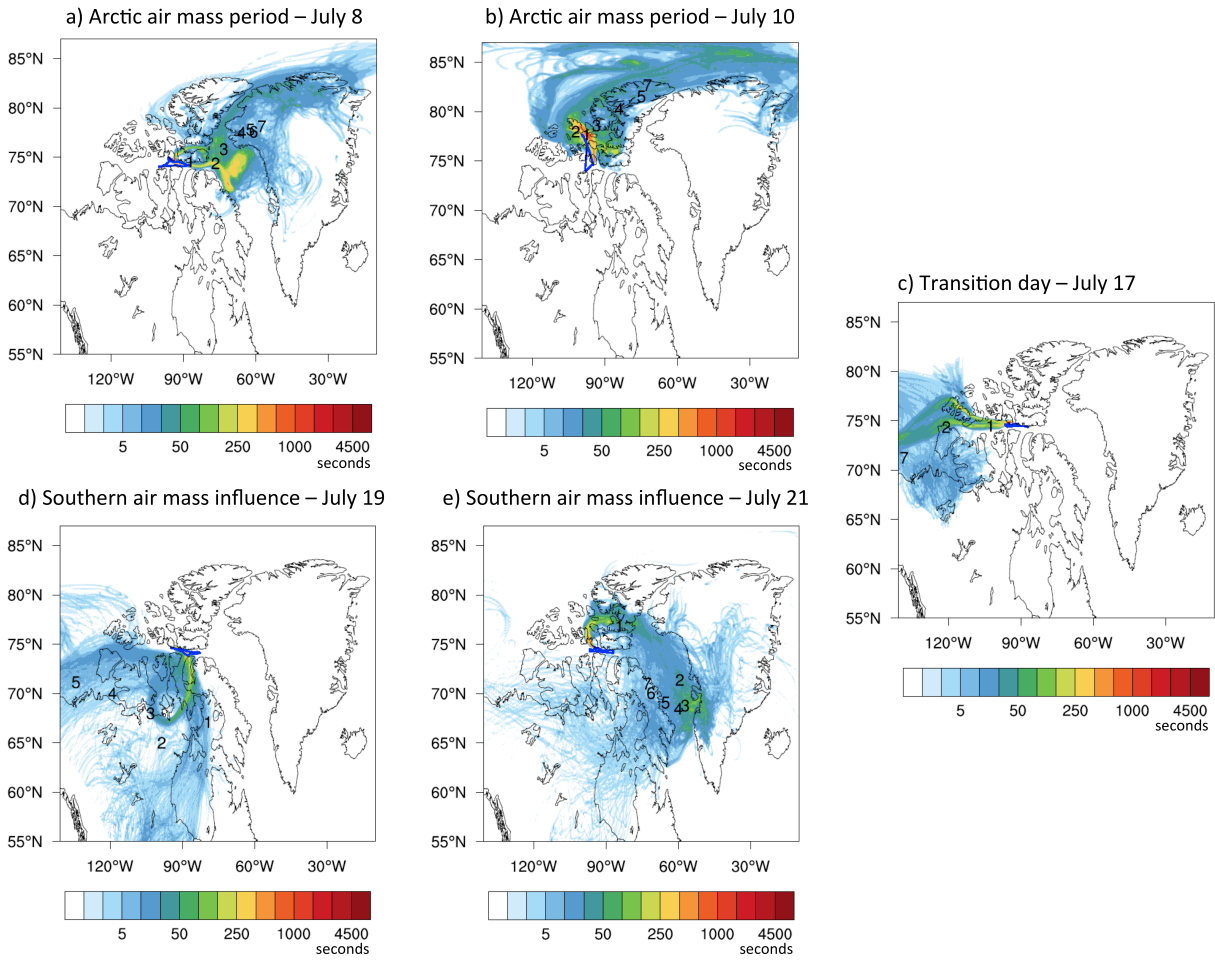
1029

1030

1031

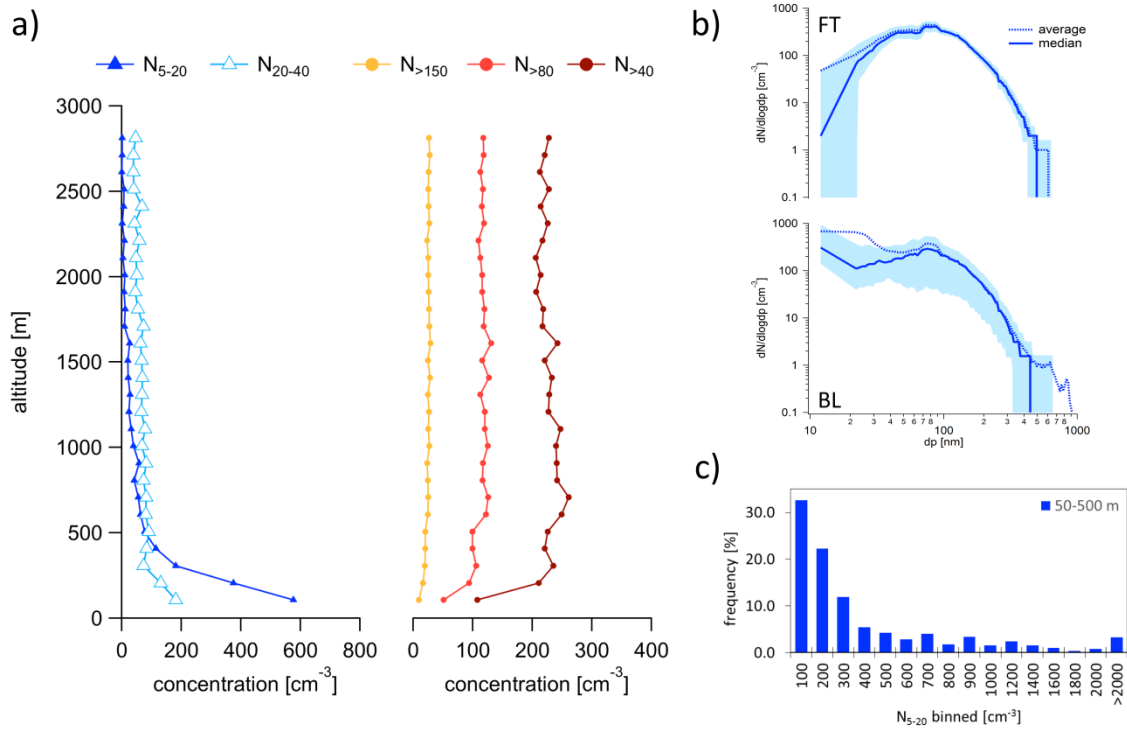


1031
 1032 Figure 3. Flight tracks colour coded by particle concentrations. a.) Flight tracks within the
 1033 boundary layer (50-300 m) colour coded by N_{tot} . b) Flight tracks within the free troposphere
 1034 (300-3000 m) colour coded by N_{tot} . c) Flight tracks within the boundary layer (50-300m)
 1035 colour coded by UFP. d) Flight tracks within the free troposphere (300-3000 m) colour coded by N_{5-20} .
 1036 e) Flight tracks within the boundary layer (50-300 m) colour coded by the ratio of N_{5-20}/N_{tot}
 1037



1038

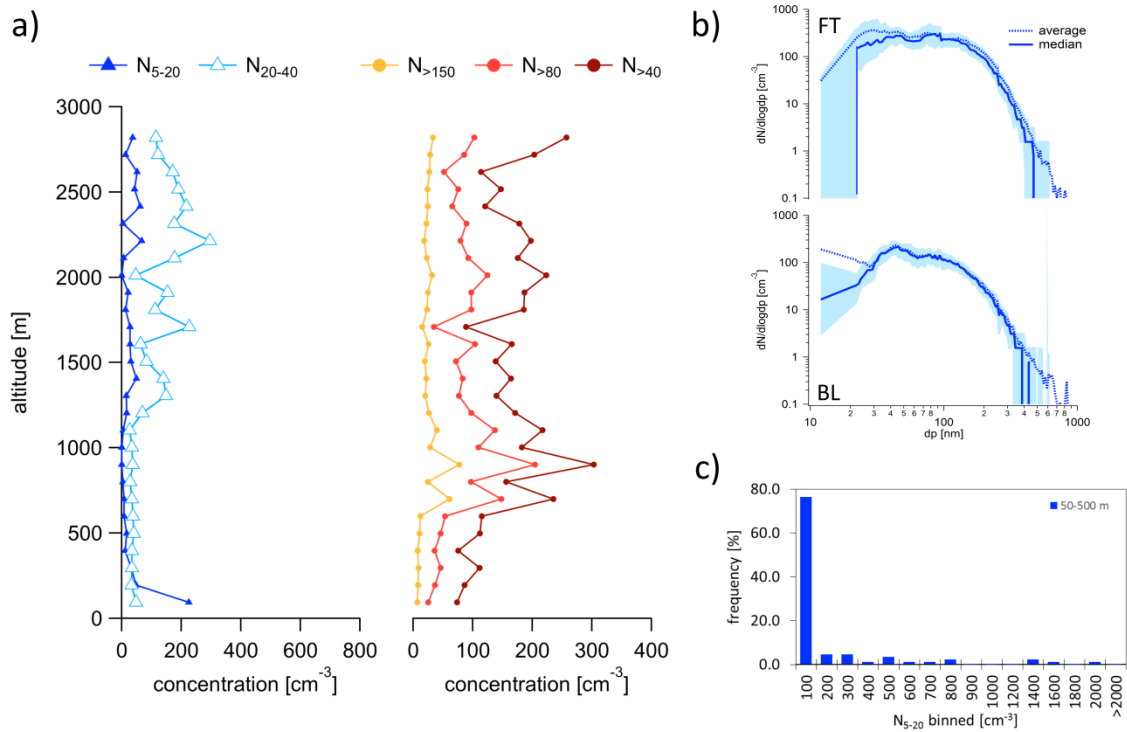
1039 Figure 4. FLEXPART-WRF potential emissions sensitivities for each flight (using particle
 1040 releases every 2 minutes along the flight track) that illustrate transport regimes during different
 1041 periods of the campaign. The colour code indicates the residence time of air in seconds and the
 1042 numbers represent the position of the plume centroid location in days prior to release (days 1-7).
 1043



1044

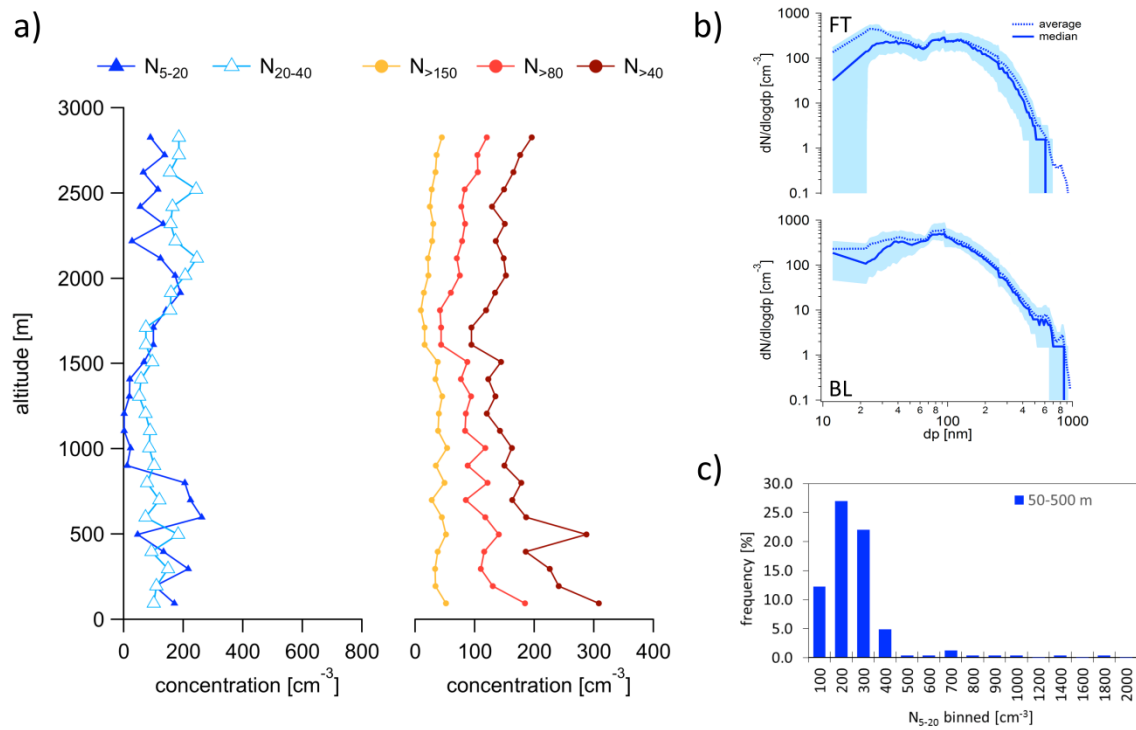
1045 Figure 5. Average particle concentration data during the Arctic air mass period. a) Average
 1046 vertical profiles of N_{5-20} , N_{20-40} , $N_{>40}$, $N_{>80}$, and $N_{>150}$. b) Average (solid line) and median
 1047 (dashed line) size distribution within the BL and the FT. The light blue area represents the 25-
 1048 75th % percentile range. c) Frequency distribution of the occurrence of UFP illustrates the large
 1049 variability of the UFP concentrations within the BL.
 1050

1050 Revised figure



1051

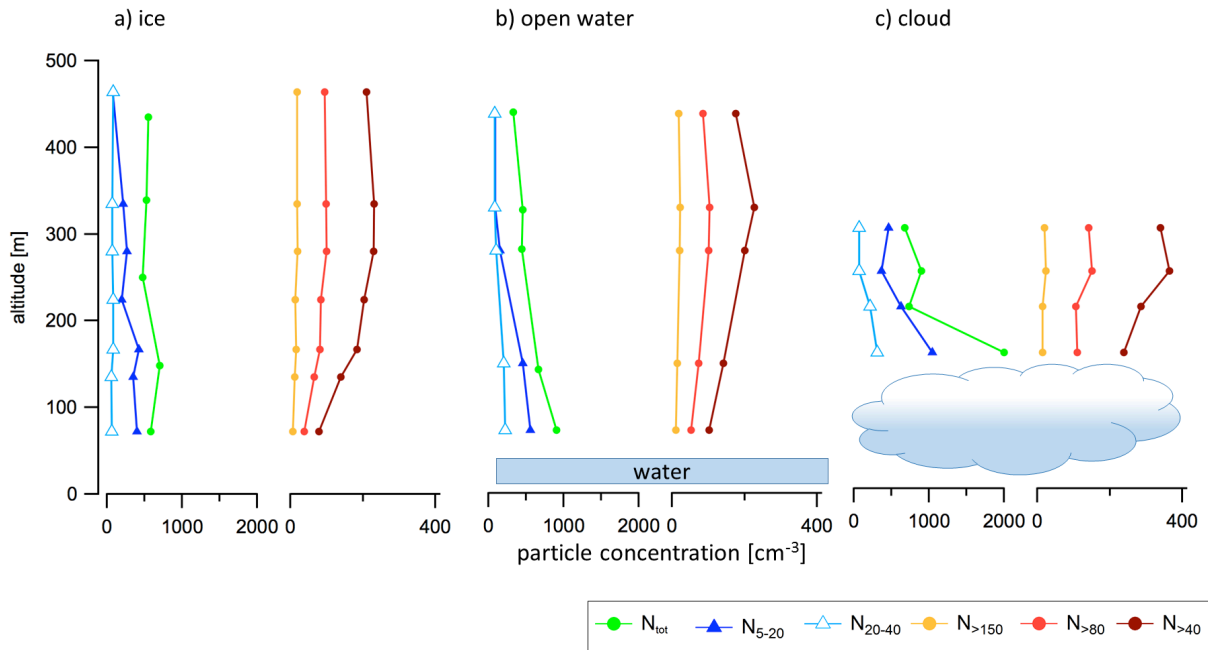
1052 Figure 6. Average particle concentration data on the transition day. a) Average vertical profiles
1053 of N₅₋₂₀, N₂₀₋₄₀, N_{>40}, N_{>80}, and N_{>150}. b) Average (solid line) and median (dashed line) size
1054 distribution within the BL and the FT. The light blue area represents the 25-75th % percentile
1055 range. c) Frequency distribution of the occurrence of UFP illustrates the large variability of the
1056 UFP concentrations within the BL.
1057



1058

1059 Figure 7. Average particle concentration data during the southern air mass period. a) Average
 1060 vertical profiles of N_{5-20} , N_{20-40} , $N_{>40}$, $N_{>80}$, and $N_{>150}$. b) Average (solid line) and median
 1061 (dashed line) size distribution within the BL and the FT. The light blue area represents the 25-
 1062 75th % percentile range. c) Frequency distribution of the occurrence of UFP illustrates the large
 1063 variability of the UFP concentrations within the BL.
 1064

1064 Revised figure

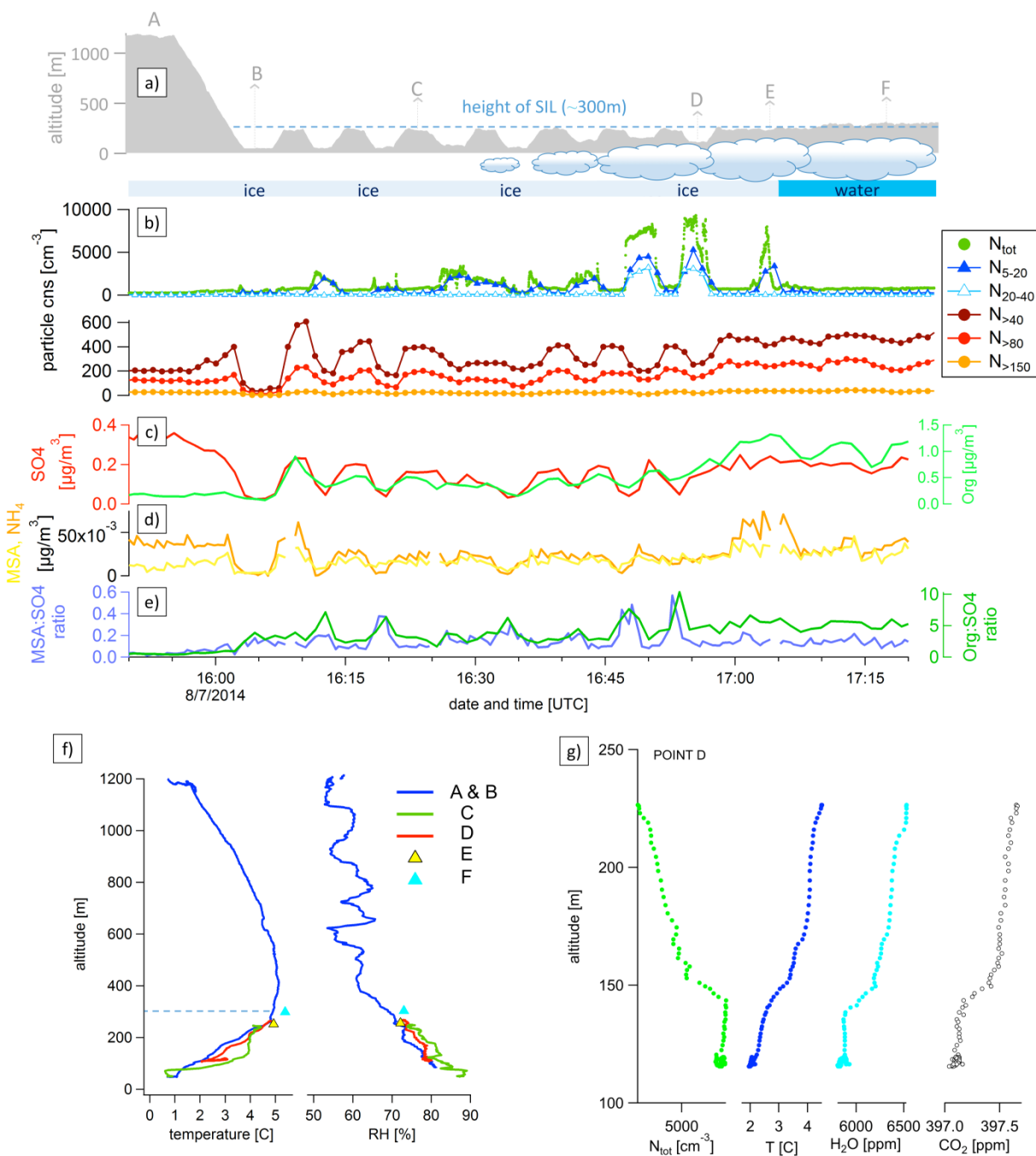


1065

1066 Figure 8. Average profiles of particle concentrations above ice, open water and cloud. The
1067 number of data points for each specific profile is: 130 above water, 216 above cloud, and 123
1068 above water.

1069

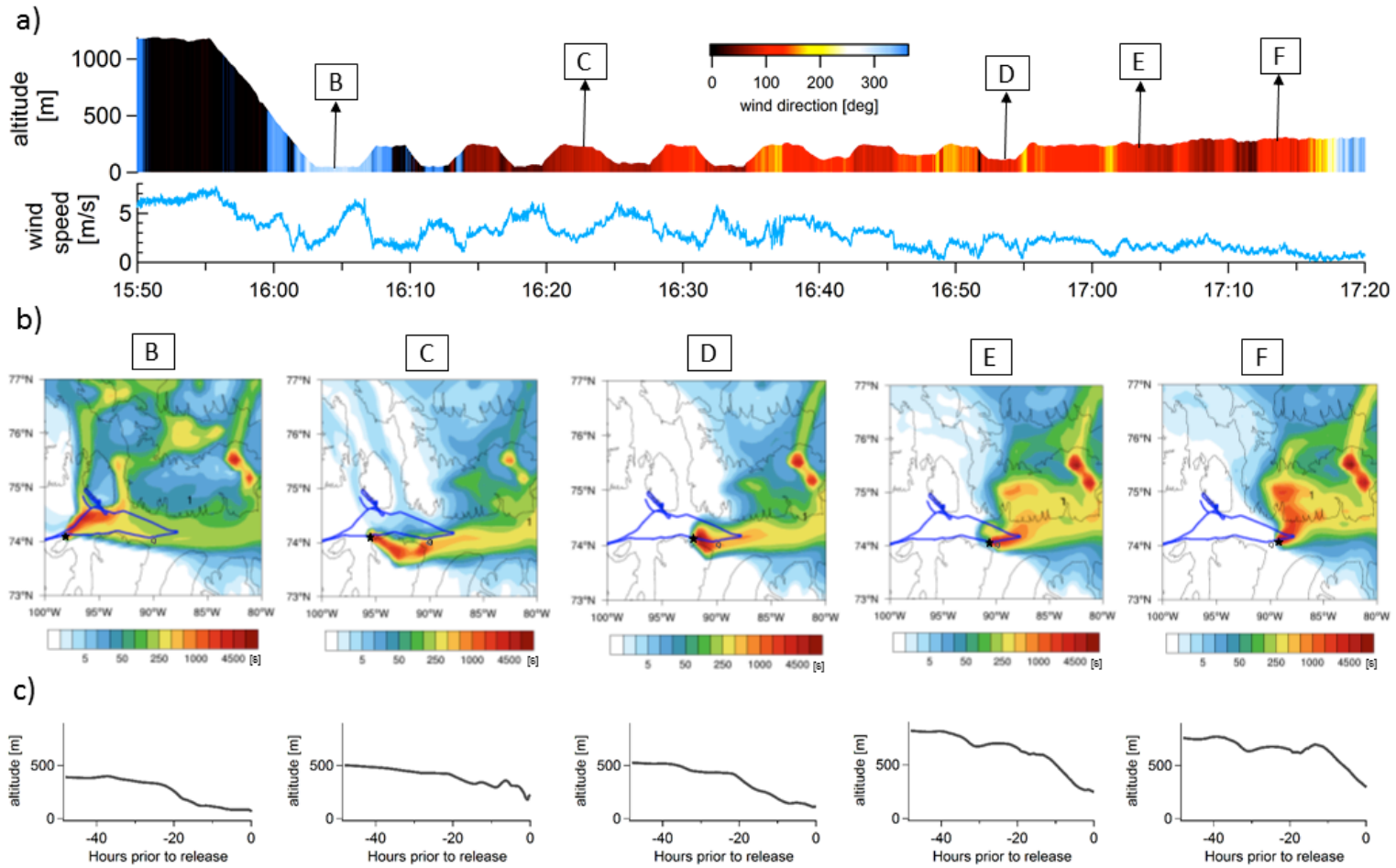
1070



1071
 1072
 1073
 1074
 1075
 1076

Figure 9. Case study from July 8 flight. Time series of flight altitude and illustration of the surface including cloud coverage (a), aerosol size (b) and chemical composition (c-e). (f) Vertical profiles of temperature and RH at locations A-F. (g) N_{tot}, temperature, H₂O mixing ratio and CO₂ profiles at location D.

1077

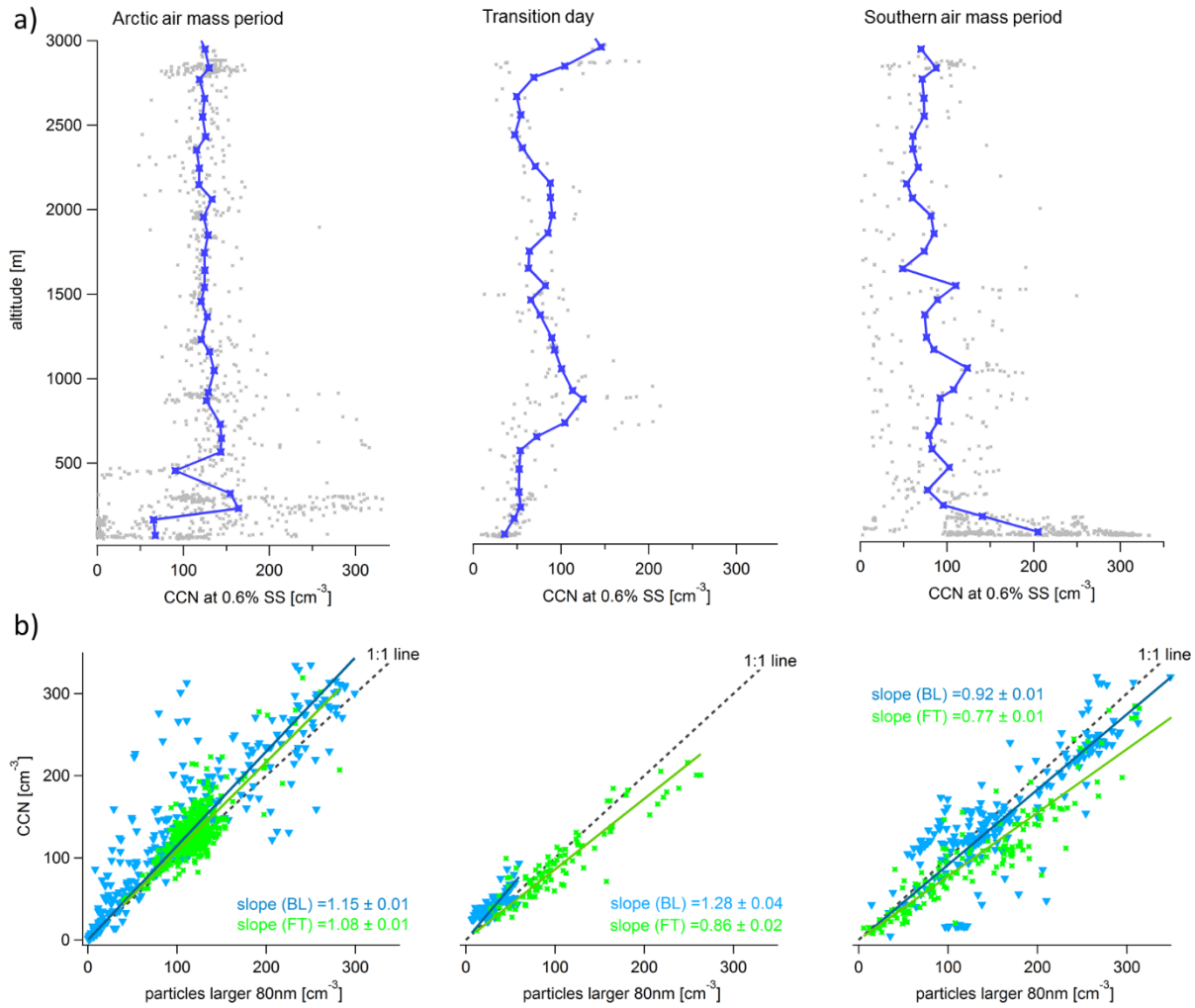


1078
1079
1080
1081

Figure 10. (a) Time series of aircraft altitude color coded with the wind direction and time series of wind speed (b) FLEXPART-WRF seven day backwards potential emissions sensitivities for points along the flight track (60 second release at time at indicated time and

1082 location) showing the air mass history at 5 representative locations within the SIL. The plume centroid location for particles with age
1083 of one day is indicated. (c) The bottom plots show the altitude of plume centroid 48 hours back in time.

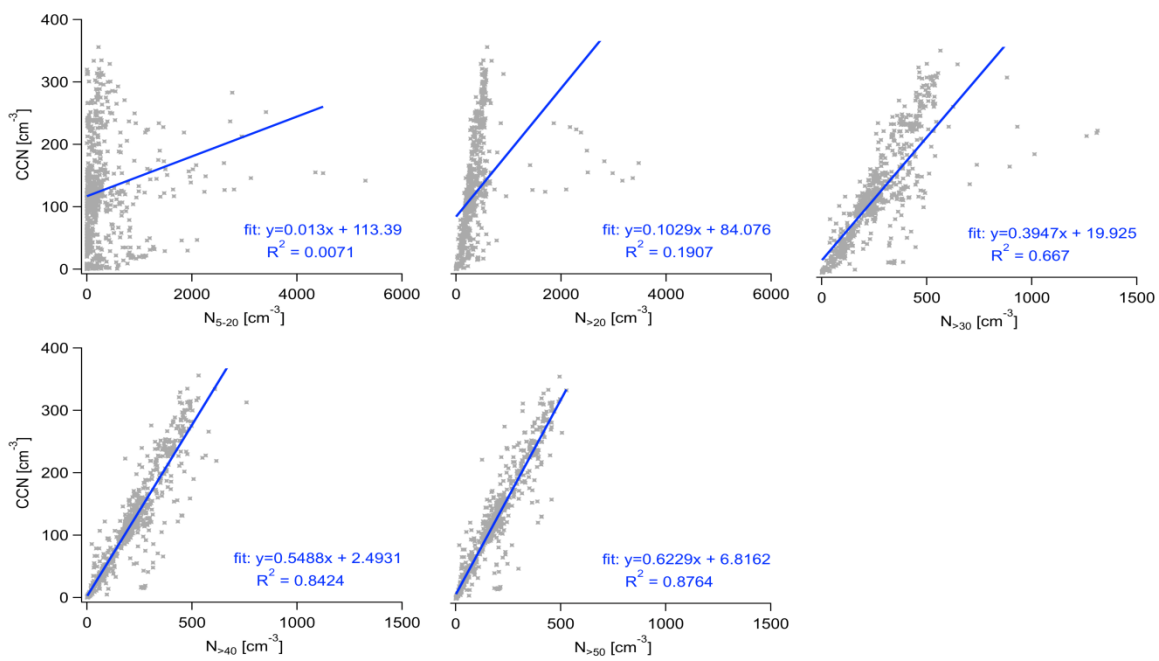
1084
1085
1086



1087
1088
1089
1090
1091
1092
1093

Figure 11. (a) Vertical profiles of average CCN concentrations (dark blue). All data points are plotted in light grey. (b) Correlation plots between CCN concentrations and particles larger than 80nm.

1093 added figure



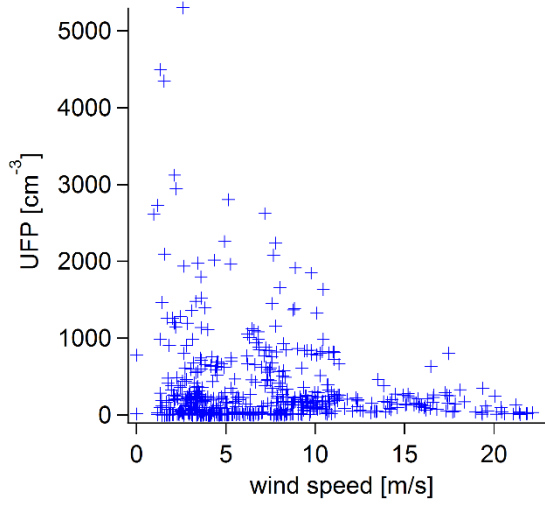
1094
1095
1096
1097
1098
1099

Figure 12. Correlations between CCN and particle concentrations for the full study period.

1099
1100

1101 **Supplemental Material**

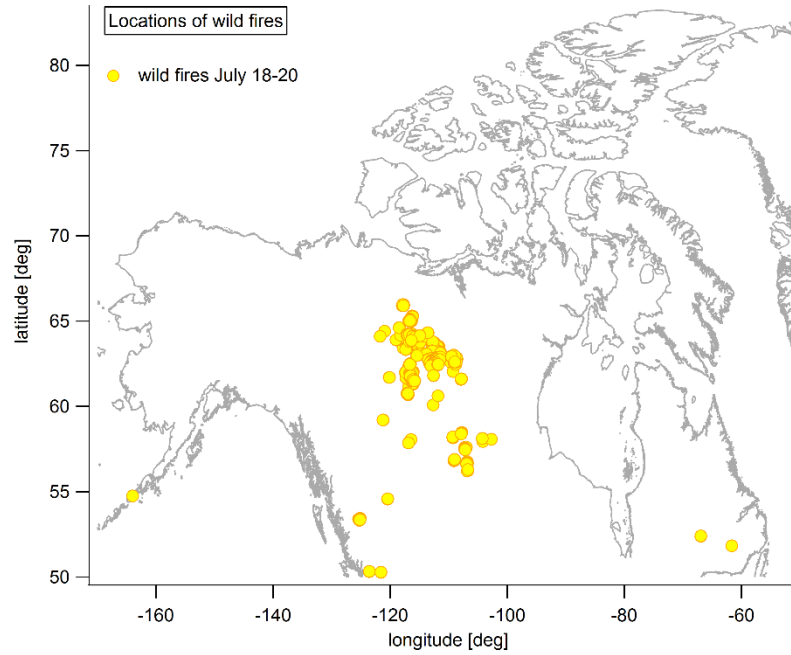
1102



1103
1104
1105
1106

S Figure 1. UFP vs wind speed within the BL for the entire campaign.

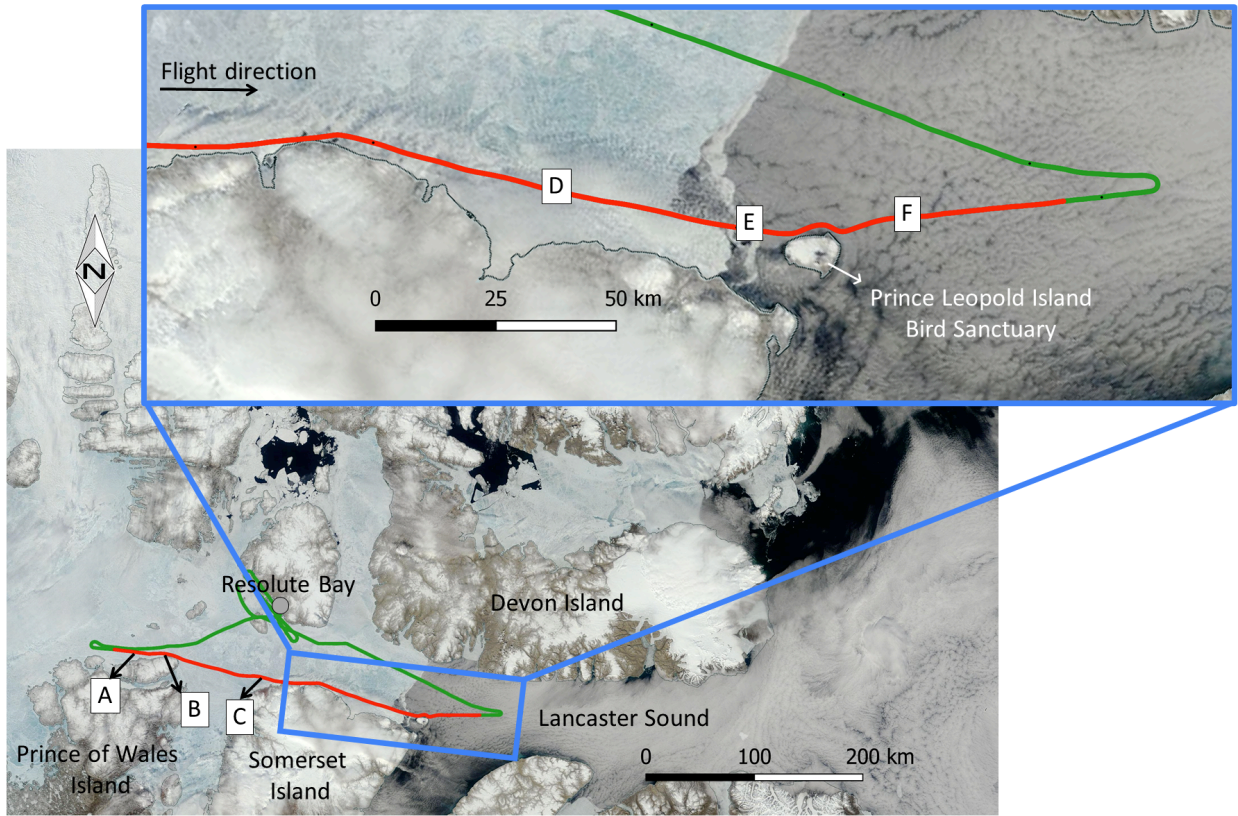
1106
1107
1108
1109



1110
1111
1112
1113
1114
1115
1116

S Figure 2. Location of wild fires relevant to the southern air mass period. The data is obtained from the NASA databank (MODIS Active Fire Detections extracted from [MCD14ML](https://earthdata.nasa.gov/active-fire-data) distributed by NASA FIRMS, available online: <https://earthdata.nasa.gov/active-fire-data>).

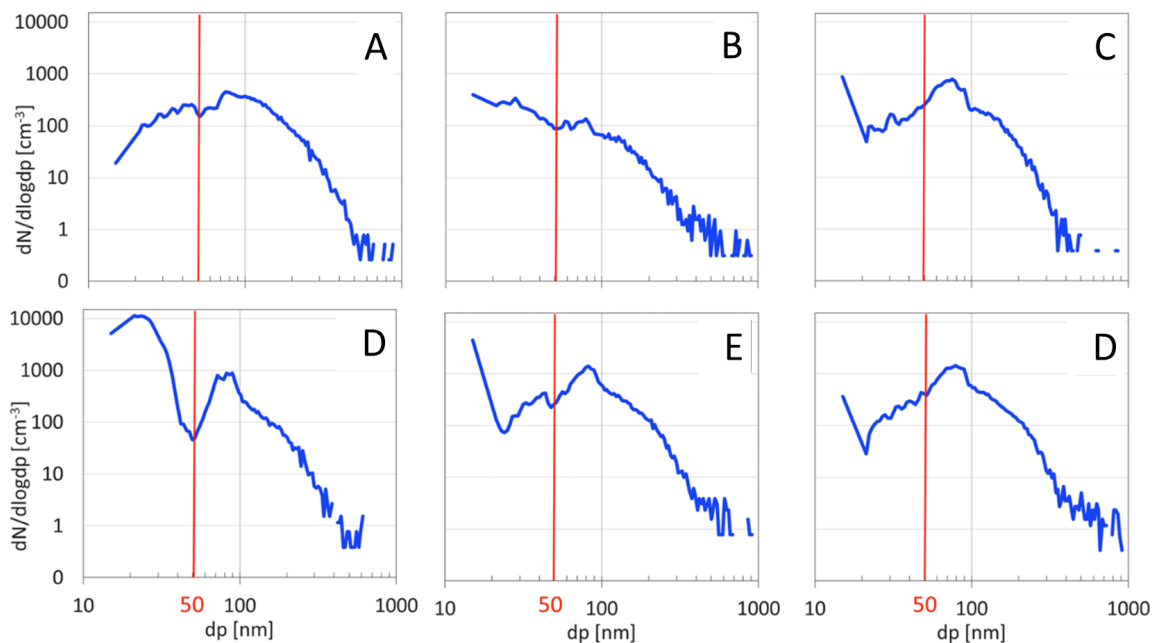
1116
1117



1118
1119
1120
1121
1122
1123
1124
1125
1126
1127
1128
1129
1130
1131

S Figure 3. Flight track of the case study on July 8. The flight track highlighted in red corresponds to the part of the flight discussed in the case study. The five locations (B)-(F) are located within the BL and air mass histories are discussed in detail. At location (A) the aircraft was still above the BL. The enlarged area shows the section where cloud patches started to reach the ice (also visible on the satellite picture) and the locations where highest concentrations of UFP were observed: (D) in cloud vicinity and (E) around the ice edge.

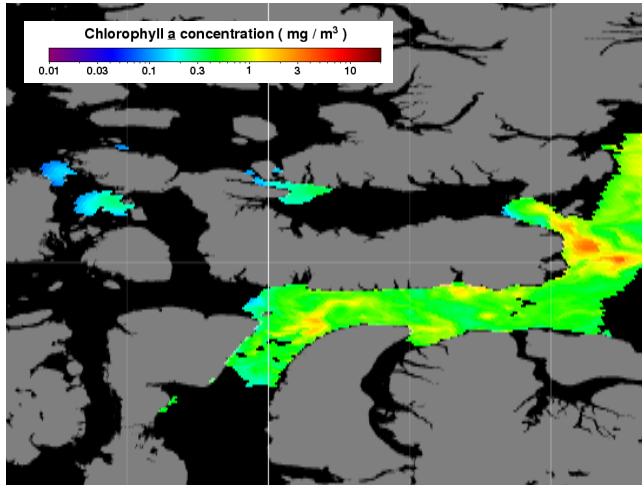
1131



1132
1133
1134
1135
1136
1137

S Figure 4. Size distributions at locations i-vi. Above the BL a mode of UFP is missing (A). The most pronounced mode of UFP was observed above cloud (D). At this time increased particle concentrations extend almost up to 50nm suggesting particle nucleation with subsequent growth.

1137
1138
1139
1140
1141
1142
1143
1144
1145



1146 S Figure 5: Chlorophyll a concentrations on July 5th 2014 estimated from satellite measurements
1147 (Visible and Infrared Imager/Radiometer Suite) by NASA
1148 (<http://oceancolor.gsfc.nasa.gov/cgi/13>).

1149
1150
1151
1152
1153